

RESEARCH OUTPUTS / RÉSULTATS DE RECHERCHE

Geological and geochemical constrains on the genesis of the sedimentary-hosted Bou Arfa Mn(-Fe) deposit (Eastern High Atlas, Morocco)

Lafforgue, Ludovic; Dekoninck, Augustin; Barbarand, Jocelyn; Brigaux, Benjamin; Bouabdellah, Mohammed; Verhaert, Michele; Mouttaqi, Abdellah; Yans, Johan

Published in:
Ore Geology Reviews

DOI:
[10.1016/j.oregeorev.2021.104094](https://doi.org/10.1016/j.oregeorev.2021.104094)

Publication date:
2021

Document Version
Version created as part of publication process; publisher's layout; not normally made publicly available

[Link to publication](#)

Citation for pulished version (HARVARD):
Lafforgue, L, Dekoninck, A, Barbarand, J, Brigaux, B, Bouabdellah, M, Verhaert, M, Mouttaqi, A & Yans, J 2021, 'Geological and geochemical constrains on the genesis of the sedimentary-hosted Bou Arfa Mn(-Fe) deposit (Eastern High Atlas, Morocco)', *Ore Geology Reviews*, vol. 133, 104094.
<https://doi.org/10.1016/j.oregeorev.2021.104094>

General rights

Copyright and moral rights for the publications made accessible in the public portal are retained by the authors and/or other copyright owners and it is a condition of accessing publications that users recognise and abide by the legal requirements associated with these rights.

- Users may download and print one copy of any publication from the public portal for the purpose of private study or research.
- You may not further distribute the material or use it for any profit-making activity or commercial gain
- You may freely distribute the URL identifying the publication in the public portal ?

Take down policy

If you believe that this document breaches copyright please contact us providing details, and we will remove access to the work immediately and investigate your claim.

Journal Pre-proofs

Geological and geochemical constrains on the genesis of the sedimentary-hosted Bou Arfa Mn(-Fe) deposit (Eastern High Atlas, Morocco)

Ludovic Lafforgue, Augustin Dekoninck, Jocelyn Barbarand, Benjamin Brigaud, Mohammed Bouabdellah, Michèle Verhaert, Abdellah Mouttaqi, Johan Yans

PII: S0169-1368(21)00119-0
DOI: <https://doi.org/10.1016/j.oregeorev.2021.104094>
Reference: OREGEO 104094

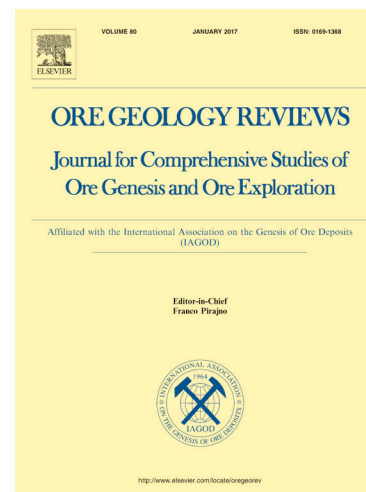
To appear in: *Ore Geology Reviews*

Received Date: 17 December 2020
Revised Date: 19 February 2021
Accepted Date: 1 March 2021

Please cite this article as: L. Lafforgue, A. Dekoninck, J. Barbarand, B. Brigaud, M. Bouabdellah, M. Verhaert, A. Mouttaqi, J. Yans, Geological and geochemical constrains on the genesis of the sedimentary-hosted Bou Arfa Mn(-Fe) deposit (Eastern High Atlas, Morocco), *Ore Geology Reviews* (2021), doi: <https://doi.org/10.1016/j.oregeorev.2021.104094>

This is a PDF file of an article that has undergone enhancements after acceptance, such as the addition of a cover page and metadata, and formatting for readability, but it is not yet the definitive version of record. This version will undergo additional copyediting, typesetting and review before it is published in its final form, but we are providing this version to give early visibility of the article. Please note that, during the production process, errors may be discovered which could affect the content, and all legal disclaimers that apply to the journal pertain.

© 2021 Elsevier B.V. All rights reserved.



1 **Geological and geochemical constrains on the genesis of the sedimentary-hosted Bou**
2 **Arfa Mn(-Fe) deposit (Eastern High Atlas, Morocco)**

3 Ludovic Lafforgue¹, Augustin Dekoninck²@, Jocelyn Barbarand¹, Benjamin Brigaud¹,
4 Mohammed Bouabdellah³, Michèle Verhaert², Abdellah Mouttaqi⁴, Johan Yans²

5 ¹Université Paris-Saclay, CNRS, GEOPS, 91405, Orsay, France.

6 ²Institute of Life-Earth-Environment (ILEE), University of Namur, 61 rue de Bruxelles B-5000,
7 Namur, Belgium.

8 ³Département de Géologie, Faculté des Sciences, Université Mohammed Premier, Avenue
9 Mohammed VI, BP 717, 60000 Oujda, Morocco.

10 ⁴Office national des Mines et des Hydrocarbures, BP 99 Rabat, Morocco.

11 Ludovic Lafforgue: ludovic.lafforgue.c@gmail.com

12 Augustin Dekoninck (corresponding author): augustin.dekoninck@unamur.be

13 Jocelyn Barbarand: jocelyn.barbarand@u-psud.fr

14 Benjamin Brigaud: benjamin.brigaud@u-psud.fr

15 Mohammed Bouabdellah: mbouabdellah2002@yahoo.fr

16 Michèle Verhaert: michele.verhaert@hotmail.com

17 Abdellah Mouttaqi: MOUTTAQI@onhym.com

18 Johan Yans: johan.yans@unamur.be

19

21 Abstract

22 Carbonate-hosted Mn deposits are widespread in North Africa with most of the Mn ores
23 being hosted by Mesozoic dolomitic formations of the Moroccan Atlasic system. The Bou
24 Arfa Mn(-Fe) deposit described herein is located in the eastern High Atlas, close to the North
25 Atlasic Front, and has accounted for the production of ~2 Mt of ore grading from 33 to 82%
26 Mn. The mineralization occurs within Sinemurian flat-lying dolostones as stratabound and
27 karst-filling (veins, lenses, pockets). This mineralization is characterized by the extensive
28 presence of pyrolusite, and minor concentrations of manganite, hausmannite, goethite and
29 hematite. Previous studies suggested that the Bou Arfa Mn-bearing mineralization has a
30 strictly syndimentary origin, but the intense dolomitization and the occurrence of Mn oxides
31 instead of Mn carbonates question this model. New petrographical, mineralogical and
32 geochemical data show that three dolomitization phases accompanied the ore formation. The
33 early syndimentary dolomitization was not responsible for strong Mn enrichments, whereas
34 a second dolomitization took place with the formation of hausmannite and manganite during
35 early diagenesis. The precipitation mechanism involves circulation of dissolved Mn^{2+} in pore
36 waters, and then precipitation under diagenetic suboxic and alkaline conditions. The scarcity
37 of Mn carbonates is likely due to competitiveness of dissolved carbonates species that have
38 favored dolomite precipitation in the early stage. Presence of saddle dolomite in a
39 subsequent alteration stage, crystallography of the Fe oxides, and evolution of $\delta^{13}C$ and $\delta^{18}O$
40 reflect burial diagenesis and fluid mixing in the carbonate host rock. These conditions have
41 enabled the transformation of the primary ore into pyrolusite, when diagenetically-derived
42 hydrothermal fluids have generated vein-filling ore. The position of the Bou Arfa site above a
43 paleohigh formed during Atlas rifting, the presence of a faulted zone and the dolomitization of
44 the Sinemurian series have delimited the extension of this diagenetic Mn deposit, which is in
45 some points similar to MVT deposits of North Africa. Weathering is poorly recorded in the
46 Bou Arfa Mn ores due to the stability of the ore-forming minerals under subaerial conditions
47 in relation to the most recent periods of exposure of the High Atlas building.

48 Keywords: manganese, Bou Arfa, diagenesis, Morocco, sedimentary-hosted

50 **1. INTRODUCTION**

51 Sedimentary-hosted Mn deposits are considered as the most significant amongst different
52 ore deposit types, because they ensure high longevity, large tonnage, and relatively high
53 average grades (Kuleshov, 2016; Laznicka, 1992; Maynard, 2014; Roy, 2006). The
54 accumulation of Mn in sediments is generally triggered by the formation of (i)
55 ferromanganese nodules above the ocean floor (Glasby, 2006; Maynard, 2014; Wang and
56 Müller, 2009), or (ii) Mn-bearing carbonates under diagenetic conditions, either from
57 precipitation in pore waters, or by replacement of Mn-rich oxides, oxyhydroxides and
58 hydroxides (hereafter referred to as Mn oxides; Johnson et al. 2016). Mn sources in
59 sediments can be either distant hydrothermal vents or hydrogenous (terrigenous) influxes
60 (Fleet, 1983; Glasby, 2006). Formation models (Calvert and Pedersen, 1996; Cannon and
61 Force, 1983; Force and Cannon, 1988; Force and Maynard, 1991; Maynard, 2014, 2010)
62 involve the precipitation of primary Mn oxides at the interface between reducing and oxidizing
63 environments. Most of these oxides are not deposited in deep sediments because they are
64 dissolved again once they deepen in the water column, unless the seafloor is shallow
65 enough to intercept the redox boundary. Iron is not involved in this process as Fe remains
66 fixed in sulfide minerals at the deeper water-sediments interface (Maynard, 2014, 2010). Sea
67 level changes may have a strong influence on the concentration and the geometry of Mn
68 orebodies (Roy, 2006). Most of the sedimentary-diagenetic Mn deposits are hosted in C-rich
69 shales and pelites (Kuleshov, 2016, 2011; Roy, 2006).

70 The Bou Arfa Mn deposit of the eastern High Atlas of Morocco (Fig. 1A) is located at the
71 junction between the High Atlas and the High Plateau domain close to the North Atlasic Front
72 (Fig. 1B). The Bou Arfa mineralization was discovered in 1912 and is the third Mn district of
73 Morocco alongside the Imini-Tasdremt (Dekoninck et al., 2016a, 2020; Gutzmer et al., 2006)
74 and the Ouarzazate mining districts (Choubert and Faure-Muret 1973; Pouit 1980; Fig. 1A).
75 Previous works have shown that mineralization mainly occurs as stratabound and karst-fill
76 within Sinemurian dolostones (Fig. 2). Their mineralogy consists exclusively of Mn oxides
77 such as pyrolusite (β -MnO₂; Pouit and Jouravsky 1965). Vein-related Mn mineralization is
78 also described and displays massive Fe oxides (goethite) alongside the Mn oxides. The
79 dolomitized host rocks are enriched up to 1–3% Mn and Pouit and Jouravsky (1965)
80 suggested that the carbonate host rocks constitute the source of manganese.

81 These features interestingly suggest the intervention of processes different from those
82 involved in giant sedimentary-diagenetic deposits (Johnson et al., 2016; Kuleshov, 2016;
83 Maynard, 2014, 2010; Roy, 2006). These high-grade Mn ores occurring in a restricted area
84 would imply epigenetic processes related to dolomitization. Pouit and Jouravsky (1965)

85 suggested a two-step model to explain the evolution of the Mn mineralization after
86 replacement of a synsedimentary carbonate precursor and their oxidation. However, this
87 model remains questionable (du Dresnay, 1965; Michard and Raddi, 2011; Pouit and
88 Jouravsky, 1965). Accordingly, the genesis of Bou Arfa Mn mineralization needs an in-depth
89 revision in order to address issues related to the syn-sedimentary, diagenetic and/or
90 hydrothermal origin of the orebodies; the link with dolomitization of the host Sinemurian
91 marine carbonates; the massive presence of Mn oxides instead of Mn-rich carbonates
92 (kutnohorite, rhodochrosite or Mn-rich calcite) and the role played by supergene processes.
93 The main objectives of this paper consist of (1) refining the mineralogy and petrography of
94 the Mn mineralization and host carbonates, and (2) defining the relation between the ore
95 formation and host carbonates. The final aim is to propose a robust metallogenic model for
96 the Bou Arfa deposit and special care is devoted to the link between mineralization and
97 dolomitization.

98 **2. REGIONAL AND LOCAL GEOLOGICAL SETTING**

99 The Atlasic fold and thrust belt is a complex structure resulting from the inversion of Triassic
100 and Jurassic basins in the frame of the Africa-Europe convergence (Choubert and Faure-
101 Muret 1962; Mattauer et al. 1977; Fig. 1A). Two main faults border the chain: the northern
102 main thrust named the “North Atlasic Front” (NAF) and the “South Atlasic Fault” (SAF). The
103 chronology of the Atlasic building follows two main phases: Eocene and Plio-Quaternary
104 (Frizon de Lamotte et al., 2009, 2000). A third Miocene phase is identified due to lithosphere
105 thinning that supports the current topography of the Anti-Atlas, the High and the Middle Atlas
106 (Gouiza et al., 2017, 2017; Leprêtre et al., 2015; Missenard et al., 2008, 2006; Seber et al.,
107 1996).

108 The Bou Arfa area is located in the eastern part of the High Atlas, close to the NAF.
109 The host rocks correspond to Paleozoic schists undetermined in age unconformably overlain
110 by a thick pre-rift Triassic succession, and Jurassic and Cretaceous syn-rift sediments. The
111 Jbel Bou Arfa (1830m; Fig 1B) forms an E-W anticline crossed by a major E-W fault (Aïn
112 Beida fault; du Dresnay 1965). This structure separates the Atlasic system in the south from
113 a non-deformed domain forming the so-called “High Plateaus” in the north (Fig. 1B). Triassic
114 to Jurassic Atlasic basins are rift basins controlled by normal faults and represent transfer
115 zone between two opening domains, namely the Central Atlantic and Tethyan oceans (Fig.
116 1A; Frizon de Lamotte et al. 2000). The E-W Aïn Beida fault is a main regional structure that
117 split the Bou Arfa area in two blocks: the northern block hosts the Ain-Beida and Hamaraouet
118 Mn mineralization, whereas the southern block hosts small Mn spots (Fig. 1B).

119 In the Bou Arfa Mn deposit, Sinemurian series are dolostones interbedded with clays
120 and thin gypsum-rich sandstones (Choubert and Faure-Muret 1962; du Dresnay 1965;
121 Salahane 1978; Fig. 2). Two main dolostone units are observed (Fig. 2). The bottom
122 dolostone called Lower “Chocolate” Unit (LCU) because of its dark brownish color is a few
123 meters thick and displays clayey levels in the upper part (du Dresnay 1965; Fig. 2). The
124 second unit, called the Upper “Chocolate” Unit (UCU), is a massive dolostone composed of
125 several strata hosting evaporitic levels, with a cumulated thickness increasing from west to
126 east (10 to 30 meters thick; du Dresnay 1965). Both are separated by an arkose level. In Bou
127 Arfa, the Pliensbachian unit unconformably overlays the Sinemurian rocks with 180 m to
128 200 m of arkoses, in which granitic boulders are observed (Fig. 2).

129 The Lower Cretaceous rocks are only observed north of the NAF and form a thin
130 reddish detrital layer. Cretaceous limestones few meters thick form the Kif El Hamar relief
131 and corresponds to an E-W syncline following the Ain Beida Fault (Fig. 1B). No Mn deposit is
132 observed in these two reliefs but Pb-Zn-Cu-V mineralization have been described (Fig. 1B;
133 Verhaert et al. 2017, 2018). Cenozoic conglomeratic lenses outcrop close to the Ain Beida
134 Fault (Fig. 1B). These lenses are witnesses of the late Cenozoic activity of the Ain Beida
135 Fault (Lafforgue, 2016).

136 **3. MATERIAL AND ANALYTICAL METHODS**

137 **3.1. Sampling strategy and methodology**

138 The Hamaraouet cliff offers a large domain of outcrops, where most of the samples were
139 collected (Fig. 1B). Mineralized orebodies and host rocks were sampled in the Hamaraouet
140 area (H1 to H4, 26 samples), in the gallery 63 (HB1, 3 samples) and in the Ain Beida site (6
141 samples; Fig. 1B; Table 1). Reference stratigraphic log and host rock samples are described
142 in barren carbonates at Hamaraouet, where neither Fe, nor Mn oxides were observed (Fig.
143 2).

144 **3.2. Analytical methods**

145 The petrography of the samples was carried out using optical microscopy,
146 cathodoluminescence (CL) microscopy (OPEA), scanning electron microscopy (SEM) and
147 Raman-microspectrometry on 70 thin sections prepared in the GEOPS laboratory (Orsay,
148 France). The description of hand specimens (Table 1) was used to select representative
149 samples for geochemical analyses and specific mineral phases from the different stages
150 defined in the paragenesis. ICP-AES and ICP-MS on bulk samples and EPMA on individual
151 minerals were used for the geochemistry. Carbon and oxygen isotope geochemistry

152 performed on carbonate phases (calcite and dolomite) was undertaken to characterize the
153 source and evolution of paleofluids.

154 3.2.1 Petrography

155 Thin sections were observed with an optical microscope Leica at a magnification between
156 x25 and x100 in plane polarized light (PPL) and in cross-polarized light (CPL).
157 Cathodoluminescence observations were made with a *Cathodyne* platine under an
158 acceleration voltage of 10 to 15 kV and a current intensity from 250 to 400 mA. Exposure
159 time was approximately 800 msec for dolomite and seconds for calcite. Texture and optical
160 characteristics have been used to define the different dolomite phases in the mineralized
161 zone. A SEM Phillips XL30 coupled with an Energy Dispersive Spectrometer (EDS) detector
162 Synergie4 PGT was used for petrographical observations and semi-quantitative analyses
163 under an acceleration potential from 15 to 25 kV and probe current of 1.5 nA.

164 3.2.2 X-ray diffraction (XRD)

165 XRD analyses were used to distinguish or correlate mineral phases, especially
166 pyrolusite and Fe oxyhydroxide mineral species. XRD data were acquired in the GEOPS
167 laboratory using a PANalytical X'Pert PRO diffractometer with X'Celerator detector and a
168 copper anticathode providing Cu $K\alpha_1$ emission ray. A Ni filter of 0.02 mm was used upon the
169 receptor. Analyses were realized on disoriented powder. All results were treated with X'pert
170 HighScore 3.0e in order to avoid induced $K\alpha_2$ rays.

171 3.2.3 Raman microspectrometry

172 Raman microspectrometry analysis was carried out at the University of Lille 1 (France)
173 in the CGCE laboratory. A Horiba Jobin-Yvon spectrometer equipped with an Ar⁺ laser was
174 used with a wavelength of 532 nm. A long acquisition time was needed for Mn oxyhydroxides
175 (~30 sec; Julien et al. 2004; Gao et al. 2009). The Ar laser spot size was between 1–2 μm
176 with variable power (max 92 mW). A filter (D1) was used in order to limit the power at
177 9.2 mW and in order to avoid phase changes due to the laser power. Raman spectra were
178 further treated with the CrystalSleuth software using the Ruff database. Peak parameters
179 were obtained with pseudoVoigt modelisation with fityk 0.8.0 software.

180 3.2.4 Geochemistry

181 3.2.4.1 Bulk-rock analysis

182 Twenty-five samples were analyzed as powders after crushing with an agate mortar at the
183 SARM laboratory (Nantes, France). An ICP-AES Jobin-Yvon JY 70 Type II was used for

184 major elements (Si, Al, Fe total, Mn total, Mg, Ca, Na, K, P, Ti and LOI). Trace elements and
185 rare earth elements were analyzed with an ICP-MS Perkin Elmer ELAN 5000 (Tables 2 and
186 3). Samples were heated at 1000 °C (fire loss) and then treated by Li tetraborate fusion to
187 determine the Lost On Ignition (LOI). Samples were analyzed after an acid dissolution (ICP-
188 AES) or a dilution (ICP-MS). Standards were routinely analyzed under the same procedure.
189 The data were compared to the Upper Continental Crust composition (Mc Donough and Sun,
190 1995) to show up enrichment or depletion. This standard was chosen as it represents the
191 best approximation for the types of rock involved in the mineralizing process at Bou Arfa.

192 *3.2.4.2 Electron Probe Microanalysis*

193 An Electron Probe Microanalysis (EPMA) CAMECA SX-Five was used for quantitative
194 analyses at the University Pierre-et-Marie-Curie of Paris (UPMC) in the Camparis Service.
195 EPMA is equipped with a LaB₆ source and five Wavelengths Dispersive Spectrometers
196 (WDS) coupled with a Bruker EDS. Acceleration potential was 15 kV and variable probe
197 current were used for the identification of minor (low current) and major elements (high
198 current). Standards and probe current are indicated in the data repository (DR1). Analyses
199 were performed on the different dolomite generations (210 spots), on the Mn (217 spots;
200 pyrolusite, hausmannite, cryptomelane, hollandite and chalcophanite) and the Fe (105 spots;
201 hematite and goethite) oxides (Tables 4, 5 and 6).

202 *3.2.5 Stable Isotope geochemistry*

203 The $\delta^{13}\text{C}$ and $\delta^{18}\text{O}$ compositions of carbonates were obtained at the Radiometric Dating and
204 Stable Isotope Research laboratory at the University of Kiel (Germany). Samples were
205 formerly collected using a micro-drill tool after an in-depth cathodoluminescence
206 characterization. Carbon and oxygen isotopic compositions were determined using 100%
207 H_3PO_4 dissolution at 75 °C with a prototype Kiel 1 unit attached to a Thermo Finnigan MAT
208 251 mass spectrometer. The results are given in the standard δ -notation, which is expressed
209 relative to V-PDB (Vienna Pee Dee Belemnite) for carbon isotopes and V-SMOW (Vienna
210 Standard Mean Ocean Water) for oxygen isotopes in permil (‰; Table 7). The reproducibility
211 of the analyses of in-house standards gave an external precision (1SD) of $\pm 0.02\text{‰}$ for $\delta^{18}\text{O}$
212 and 0.01‰ for $\delta^{13}\text{C}$.

213 **4. RESULTS**

214 *4.1 Dolomitization*

215 Dolomitization is the main form of wall-rock alteration and three stages are distinguished: (i)
216 extensive syn-sedimentary to early diagenetic replacement dolomite, (ii) epigenetic ore-stage

217 and (iii) hydrothermal dolomite superimposed on the diagenetic dolostone (Fig. 4). Regional
218 dolomitization predates mineralization and significantly enhances porosity and permeability
219 of the host rock. Ore-related dolomites occur as pore-filling or veins crosscutting the host
220 dolostone.

221 4.1.1 Barren Upper Chocolate Unit (UCU)

222 Three facies are recognized in the Upper Chocolate Unit (UCU; from bottom to top): (i)
223 sandy dolostone, (ii) massive fine-grained dolostone and (iii) bedded dolostone with bird
224 eyes (Fig. 2). (i) The UCU starts with a thin level (<50 cm thick) displaying a high proportion
225 of detrital elements including quartz, K-feldspar, and muscovite with subordinate apatite and
226 Ti oxides. These elements are cemented by an anhedral coarse-grained dolomite (Fig. 3A).
227 CL exhibits a red color in the dolomite crystals. (ii) The main facies of the UCU, where most
228 of the ore is located, is formed by a massive dolostone. The lower facies consists of a coarse
229 dolostone where sedimentary textures (pellets, oolites and pisolites) are partly preserved
230 (Fig. 3B), and partially replaced by well-developed cloudy microsaccharoidal to millimetric
231 planar dolomite crystals (Fig. 3C). Pisolites have a single to multiple-nuclei structure with
232 lightly colored columnar microbial laminations. No Mn- or Fe-rich oolites (or nodules) nor
233 laminations are observed. (iii) In the upper facies of the UCU, bird eyes are the main feature
234 (Fig. 3D). This level is composed of a micritic brownish dolomite, similar to the dolomite of
235 the bottom detrital level and of the well-preserved part of the massive dolostone level. Bird
236 eyes are filled by a clear sub-planar dolomite with a dark reddish luminescence, while
237 dolomitic cloudy rhombs coating bird eyes have a red luminescence. A small detrital fraction
238 (quartz, feldspar, Fe-Ti oxides, apatite, zircon) is also observed. On top of this level, a
239 dedolomitized limestone (Figs. 3E and F) is observed beneath the unconformity with
240 Pliensbachian arkoses (Fig. 2).

241 At distance from the mineralized zone — ~4 km south of the Aïn Beida fault in the Jbel
242 Bou Moktha — (Fig. 1B), the Sinemurian series display a well-exposed platform margin
243 system with a north-south lateral facies evolution from (1) lagoonal peloidal-ooloidal
244 dolostones to (2) bioclastic/oolitic grainstones (shoal) and finally to (3) marl/limestone
245 alternation (upper slope). This outcrop in the Jbel Bou Moktha allows to precisely locate the
246 bioclastic/oolitic shoal, protecting the lagoon to the open marine environment. At this
247 location, the lateral equivalent of the UCU only displays an early generation of micritic
248 dolomite followed by several calcite cements (Figs. 3G and H).

249 4.1.2 Carbonates phases associated to the ores

250 The three ore-related dolomite phases are not observed outside the mineralized area. Table
251 8 shows the key identification criteria for the dolomite phases.

252 4.1.2.1 *Early diagenetic dolomite phase (Dol-1)*

253 The earliest dolomitic phase (labeled Dol-1a) replaces calcite precursor, here peloids
254 or ooids. Dol-1a is micro-saccharoidal with red color in CL (Figs. 3A and B). Dol-1b
255 precipitates around Dol-1a with a similar luminescence, unzoned in CL (Fig. 3B). Dol-1a and
256 Dol-1b are the most common carbonate phases.

257 4.1.2.2 *Ore-related epigenetic to hydrothermal dolomite phases (Dol-2 and Dol-3)*

258 Coarse grain dolomite phases (Dol-2 and Dol-3) are intimately related to the highly
259 recrystallized part of the massive dolostone and to the mineralization (Figs. 3C). None of
260 these dolomites occur in the unmineralized zone. Dol-2a is a cloudy dolomite related to the
261 dissolution of sedimentary elements in the massive dolostone and forms mostly planar to
262 sub-planar rhombs with size of ~10–20 μm , cloudy in PPL and bright orange, unzoned in CL.
263 Dol-2a is intrinsically associated with another phase (Dol-2b), which is likely related to the
264 alteration of Dol-2a as shown by impregnation of Dol-2b into Dol-2a (Figs. 3C). Dol-2b is a
265 void and vein filling dolomite, much clearer than Dol-2a in PPL, and characterized by well-
266 developed (hundred microns) sub-planar to non-planar rhombs, bright greenish-yellowish
267 zoned in CL. Dol-2b is a blocky cement but is also connected to veinlets (Fig. 3C).

268 The last dolomite phase (Dol-3) is observed as cement and vein- or breccia-filling. Dol-
269 3a replaces Dol-2b and forms either a clear dolomite in PPL and dark in CL, or a dark cloudy
270 dolomite (Fig. 3C), bright red-orange unzoned in CL (Fig. 3F). Dol-3b is a clear sub-planar to
271 non-planar (saddle) coarse (hundred microns) rhomb dolomite. A zoned to unzoned dark
272 reddish luminescence characterizes Dol-3b.

273 4.1.2.3 *Late meteoric calcite phases*

274 Late calcite phases also occur across the whole sedimentary series filling the remaining
275 porosity and cutting-across the host dolostone as mm-sized veins. Two generations of calcite
276 are distinguished. The first one (Cal 1) displays yellowish color in CL with zoned
277 scalenohedron crystals in fractures and as replacement of a former dolomite crystal
278 (dedolomite). The second (Cal 2) postdates Dol-3 and is extinct in CL forming sparitic to
279 anhedral crystals in fractures or in breccia (Fig. 3E and 3F).

280 4.2 *Ore mineralogy and petrography*

281 Crosscutting relationships and mineral assemblages indicate the presence of two
282 distinct stages of Mn mineralization (Fig. 4). Veins systematically crosscut both the
283 replacement and karst mineralization. Hausmannite and manganite crystals are crossed or
284 replaced by pyrolusite and later by goethite. It suggests the existence of a prior
285 mineralization related to the formation of Mn(II) and Mn(III) oxides and the existence of two
286 Fe oxyhydroxide stages (Gth1 and Gth2).

287 4.2.1. Macroscopic features of the Mn-Fe mineralization

288 From 1922 to 1966, the Bou Arfa manganese deposit was one of the main Mn
289 producers in Morocco with a final production of about ~2 Mt Mn (Mouttaqi et al., 2011). The
290 Mn ore produced metallurgic Mn (33% Mn, 17% Fe) and chemical Mn (82% Mn, <3% Fe;
291 Pouit 1964, 1980; Pouit and Jouravsky 1965; Michard and Raddi 2011; Mouttaqi et al. 2011).
292 The mine remains closed since the seventies. The main mining site is located at Aïn Beida
293 with significant underground works (Figs. 1 and 3). The ore is also well exposed along the
294 Hamaraouet cliff (Figs. 1B and 5A), which constitutes an erosion limit between the basement
295 and the cover; minor mining activities are still in place but galleries in the Upper Chocolate
296 Unit (UCU) are preserved (Figs. 5A and B). From Aïn Beida to Hamaraouet, the Mn
297 mineralization occurs as: (1) a continuous 1-6 meters thick stratabound orebody (~2 km) by
298 replacement of the UCU (Fig. 5C), and (2) veins, stockworks, breccia karst-like (pockets,
299 lenses, cluster) mineralization filling open spaces (Figs. 5D-H; Pouit and Jouravsky 1965;
300 Pouit 1980). This second mineralization is the most important in terms of tonnage and grade.
301 It intensifies toward the core of the Bou Arfa anticline (Fig. 1B) and follows a NE-SW
302 direction parallel to Atlasic directions. It can be subdivided into three sub-groups:

- 303 (i) The main sub-type is a prismatic karst-like mineralization forming vertical pipes formerly
304 attributed to the “run-type” ore (Pouit and Jouravsky, 1965). This mineralization is ~100
305 m long and corresponds to karst collapse structure composed by dolostone blocks
306 embedded in the Mn-Fe mineralization (pyrolusite, manganite, psilomelane, goethite and
307 hematite) and secondary Mn carbonates (Mn-calcite and rhodochrosite). Their main axis
308 follows an ENE direction. According to Pouit and Jouravsky (1965), veins of various
309 sizes (Figs. 5F and 5G) and Mn stockworks (Fig. 5H) are also connected to this
310 mineralization.
- 311 (ii) Tabular karst-like mineralization (Fig. 5C) are ten meters long and wide with a thickness
312 of several meters. It follows a sedimentary discontinuous/erosive surface in the upper
313 part of the massive dolostone level of the UCU (Fig. 2) and corresponds to a network of
314 metric channels, parallel to the Sinemurian dolostone strata.

315 (iii) Finally, local veins are described through the Upper Pliensbachian sandstone. Despite
316 the local specificity of this poorly extended mineralization, Pouit and Jouravsky (1965)
317 indicate that it is likely related to a main fault. Impregnation of stratabound pyrolusite is
318 related to this vein (Figs. 5F and 5G).

319 The Bou Arfa mineralization is a mixed Mn-Fe type (25% Mn, 10-12% Fe in the bulk ore)
320 dominantly composed of pyrolusite with manganite in the deeper zone, and locally coronadite
321 group minerals (coronadite, hollandite and cryptomelane). Goethite and hematite are
322 systematically present, sometimes forming massive veins (Fig. 5F). Gangue minerals are Mn
323 carbonates, quartz, calcite and barite (Pouit, 1980).

324 4.2.2 Replacement mineralization

325 The replacement mineralization is mainly composed of pyrolusite (Fig. 5C),
326 crosscutting and replacing Dol-1b or Dol-2 (Fig. 6A). Pyrolusite occurs as elongated cleaved
327 prismatic crystals with bipyramidal sections (Fig. 6B). Several micrometric disoriented
328 needles of pyrolusite filling voids are present at the base of prismatic pyrolusite crystals (Fig.
329 6C), which means at least two generations of pyrolusite. Pyrolusite grows onto sub-planar to
330 non-planar altered crystals of Dol-2b. Dol-3b cements pyrolusite (Fig. 6B).

331 Raman peaks of pyrolusite (Julien et al., 2002, 2004) are identified with a broad shape
332 around $538 \pm 5 \text{ cm}^{-1}$ and $750 \pm 5 \text{ cm}^{-1}$ (Fig. 6D). An additional peak close to $630 \pm 5 \text{ cm}^{-1}$ is
333 also measured. The peak broadening and the presence of an additional peak at $630 \pm 5 \text{ cm}^{-1}$
334 are characteristic of slight deviations of the lattice and especially to de Wolff defects
335 corresponding to additional corner-sharing $[\text{MnO}_6]^{8-}$ octahedra (such as in 1×2 tunnel oxide
336 structure; de Wolff 1959; Julien et al. 2002). Other phases are also present in the
337 stratabound orebodies such as colloform Fe oxides (goethite) and some phyllosilicates
338 (smectite or biotite in EDS analyses). Colloform goethite crystals are surrounded by micro-
339 pyrolusite (Fig. 6E).

340 4.2.3 Karst and vein-related mineralization

341 The Hamarouet karst mineralization is mainly composed of Mn oxides and to a lesser
342 extent of Fe oxyhydroxides. Hausmannite forms euhedral crystals crosscut by Dol-3 (Figs.
343 7A and B). Hausmannite is ribbed by cleaved pyrolusite crystals that fill fissures with
344 cryptomelane (7A and B). Hausmannite is replaced by chalcophanite or cryptomelane (Figs.
345 7A and B). The iron mineralization is composed of centimeter rubbed dark goethite (with
346 hematite) crosscut by calcite. This mineralization has a colloform habit and evolves to micro
347 specular at the borders of the Mn ore (Fig. 7E). Fe oxyhydroxides also form a continuous
348 uniform reddish level surrounding lenticular mineralization and are mostly related to the

349 prismatic karst (Fig. 5G). These reddish levels are composed of micro disoriented needles of
350 pyrolusite replacing large Dol-2b rhombs.

351 Colloform early manganite (γ -MnOOH) occurs as planar crystals of ten to a hundred
352 microns (Figs. 7C and D). These crystals form lenticular masses with rare hausmannite and
353 barite crystals (Fig. 7D). Manganite is only observed in Aïn Beida.

354 Carbonate phases are also associated to the Mn-bearing ore minerals and are similar to
355 those observed in the host-rock. Dol-2b, Dol-3 and late calcite phases are observable (Figs.
356 3F, 7A and B). The late stage calcite is also associated with the precipitation of P-rich
357 minerals (apatite) and some phyllosilicates (smectite or biotite; Fig. 3E). Dol-2b crisscrosses
358 manganite-hausmannite phases at Aïn Beida, when Dol-3 fills voids (Fig. 7A) and surrounds
359 hausmannite. In Aïn Beida area a late Ca-rich rhodochrosite, partially replacing manganite
360 and Dol-2b crystals is observable (Fig. 7C and D).

361 4.2.4 Crystallinity of the Fe oxides

362 According to the Scherrer formulation (Langford and Wilson, 1978; Scherrer, 1918), the
363 average size of the crystallite populations of hematite and goethite ranges between 0.02 and
364 0.12 μm in the whole dataset (Fig. 8). These values were measured at the maximum width of
365 each crystal or in the middle of the crystal and are in good agreement with different studies
366 (Cornell and Schwertmann, 2003; Gualtieri and Venturelli, 1999; Rendon et al., 1983;
367 Schwertmann et al., 1985). The crystallite size of hematite in the stockwork mineralization of
368 Bou Arfa is close to a proto-hematite. This type of hematite is a non-stoichiometric phase,
369 which is characteristic of the transformation by dehydration of goethite into hematite beyond
370 140 °C in laboratory experiments (Gualtieri and Venturelli, 1999; Pomiès et al., 1998; Walter
371 et al., 2001; Wolska and Schwertmann, 1989; Wolska and Szajda, 1988). This proto-
372 hematite is not an authigenic phase and possesses two distinct groups of crystallites (Lima-
373 de-Faria, 1963). Schwertmann et al. (1985) have shown that the dimension of the a-cell
374 parameter is a witness of the formation temperature of goethite. A long distance
375 ($4.626 \pm 0.005\text{Å}$) refers to a low temperature of formation (4–40°C), whereas a shorter
376 dimension ($4.610 \pm 0.001\text{Å}$) corresponds to higher temperatures (50–90°C). The cell
377 dimensions of four Bou Arfa goethites (Table 9) recovered from the reticular distance of
378 planes (200), (040) and (111) are close to a synthetic goethite crystallized at 50 °C. It is also
379 worth noting that a decrease in the peak intensity of 2.45Å is characteristic of goethite
380 formed at >40 °C (Schwertmann et al., 1985), which is actually the case in Bou Arfa goethite
381 (see DR2).

382 4.3. Geochemistry

383 4.3.1 Mineral chemistry

384 4.3.1.1 Carbonates

385 EPMA results on dolomite and calcite are reported in Table 4 and plotted in Fig. 9. All
386 the dolomitic phases show excess Ca (26.3 wt.% to 37.8 wt.%; Figs. 9A and B; Table 4). No
387 significant variation is observed to distinguish most of the different generations of dolomites
388 (Figs. 9A and B). Only vein-filling Dol-3 significantly differs from the others, as it contains the
389 highest MnO content (between 1.21 and 9.03 wt.%; Table 4). MnO enrichment implies that
390 late dolomite is close to kutnohorite. It is worth emphasizing that although FeO content (0.13
391 to 1.11 wt.%; Table 4) is lower than MnO, the absolute FeO/MnO ratio is lower than for most
392 of the sedimentary dolomites (Fig. 9C; Searl and Fallick 1990; Montanez and Read 1992;
393 Gasparria et al. 2003; Fu et al. 2006). The total amount of trace elements slightly
394 decreases from Dol-1 to Dol-3. The Sr concentration is lower than common marine
395 carbonates (Brand and Veizer, 1980; Zenger et al., 1980). The two late calcite phases are
396 also distinguished, one is Fe-rich, whereas the other is Mn-rich.

397 4.3.1.2 Manganese oxides

398 Hausmannite displays minor amounts of SiO₂ (0.05 to 0.30 ± 0.01 wt.%), ZnO (0.05 to
399 2.08 ± 0.02 wt.%) and Fe₂O₃ (0.55 to 1.55 ± 0.24wt.%). Other elements such as Na₂O, MgO,
400 Al₂O₃ or SrO are present at very low concentrations. As hausmannite is commonly replaced
401 by chalcophanite (Fig. 6F), some of the EPMA compositions may be affected.

402 The composition of pyrolusite is heterogeneous. All pyrolusite contain substantial
403 amounts of Al₂O₃ (5.75 ± 0.03 wt.%), SiO₂ (2.11 ± 0.03 wt.%) and CaO (2.25 ± 0.05 wt.%).
404 Only the late-stage pyrolusite grains contain significant amounts of MgO (0.06-1.63 wt.%)
405 and K₂O (0-2.27 wt.%). Pyrolusite in stratabound ores (gallery 63) shows a low CaO content
406 (0.20 ± 0.06%) and the highest Al₂O₃ (0.89 ± 1.12 wt.% to 1.30 ± 0.53 wt.%). All the vein-
407 related pyrolusite have a homogeneous composition.

408 EPMA analyzes also reveal that coronadite group minerals – here represented by
409 hollandite and cryptomelane following the nomenclature of Biagioni et al. (2013) –,
410 concentrate Ba, Sr, K, Ca and Mg (Table 5). K, Ba and Mg are the dominant cations and only
411 hollandite is observed as a pure end-member. Chalcophanite sometimes displays very low
412 Zn concentration, instead of Mg, which could be dominant (up to 4.89 wt.%).

413 4.3.1.3 Goethite and hematite

414 All analyzed hematite and goethite samples are from Hamaraouet (Fig. 1B). The total
415 Fe₂O₃ content is abnormally low for goethite and hematite (Table 6) in comparison with their

416 ideal formula. The total Mn_2O_3 and SiO_2 contents delimit two geochemical trends: (i) The
417 massive colloform goethite and the Fe oxides associated with dedolomitization are enriched
418 in Mn_2O_3 (mean values from 1.46 ± 0.24 to 2.30 ± 0.10 wt.%; Table 6) with minor SiO_2 (mean
419 values from 0.11 ± 0.06 to 0.49 ± 0.47 wt.%) and; (ii) The goethite in veins are enriched in
420 SiO_2 (mean values from 1.71 ± 0.14 to 3.50 ± 0.4 wt.%) with minor Mn_2O_3 content (mean
421 values from 0.09 ± 0.01 to 0.16 ± 0.02 wt.%; Table 6). Goethite and hematite also exhibit
422 minor concentrations of Al_2O_3 , MgO , CaO , P_2O_5 and K_2O (ranging from 0.02 to 0.75 wt. %).

423 4.3.2 Bulk-rock and Mn-ore geochemistry

424 The Sinemurian dolostones display similar geochemical patterns irrespective of the
425 dolomitizing event that affected these rocks (Fig. 10A). The presence of detrital phases such
426 as quartz, feldspars, zircon, monazite and Ti-oxides explains some high immobile and
427 lithophile contents. One of the striking features in all samples is the higher MnO content (0.74
428 to 4.71 wt.%) comparative to FeO (0.26% to 1.44 wt.%; Fig. 10A; Table 2). The enrichment in
429 As is also significant.

430 The karst Mn ores of Aïn Beida, the stratabound Mn and Fe orebodies and the fracture-
431 filling Fe-Mn mineralization show a similar geochemical signature despite their different
432 mineralogy (Figs. 10A and B). Geochemical patterns are close to those of the host rock but
433 with relatively higher enrichments. Lithophile (V), chalcophile (Pb, Zn, Cu) and siderophile
434 (Co, Ni, Mn) elements are more enriched than in the host rock (Fig. 10A). Ba, As, Zn and Fe
435 contents differ between samples: higher Ba and As contents are recorded at Aïn Beida. The
436 Mn/Fe ratio of samples from Aïn Beida ($\text{Mn}/\text{Fe}_{\text{AB1}} = 66.9$; $\text{Mn}/\text{Fe}_{\text{AB2}} = 1.3$, Table 3) is also one
437 of the lowest. The late supergene weathered ores are enriched in Sr (1316 to 2350 ppm), Zn
438 (1446 to 2136 ppm) and K_2O (0.66 to 0.96 wt.%), likely due to the presence of hollandite,
439 cryptomelane and chalcophanite. Concentration in lithophile, immobile elements and in REE
440 are low compared to the host rock (Fig. 10A).

441 The enrichments of the Fe-rich ores are roughly the same as for the Mn ore with some
442 increase in V, As and Pb in the vein-related hematite of Hamaraouet (Fig. 10B). This
443 mineralization is also enriched in Be (6 to 114 ppm) and Ge (2 to 124 ppm). The Fe ore has
444 also a high Mn content up to 0.14-1.07 wt.% $\text{Fe}_2\text{O}_{3\text{t}}$ (Table 3).

445 Overall, As and Mn are enriched in both the host dolostone and in the mineralization
446 (Tables 2 and 3). Paleozoic schists are depleted in Mn (0.02 wt.% MnO). Chalcophile
447 elements (As, Pb, Zn, Cu) are abundant in the Mn ores and in most of the Fe ores (Fig. 10A
448 and B; Table 3).

449 4.3.3 Carbon and oxygen isotopic compositions of carbonates

450 The analyzed carbonates show a wide range of carbon and oxygen isotopic
451 compositions with $\delta^{13}\text{C}_{\text{VPDB}}$ and $\delta^{18}\text{O}_{\text{VSMOW}}$ ratios ranging from -8.6 to 2.2‰ and 17.3 to
452 29.8‰, respectively (Fig. 11; Table 7). $\delta^{18}\text{O}_{\text{VSMOW}}$ and $\delta^{13}\text{C}_{\text{PDB}}$ ratios for the primary Dol-1
453 phase are rather homogenous clustering around 29.2‰ and 29.8‰ for $\delta^{18}\text{O}_{\text{VSMOW}}$ and 0.1‰
454 to 2.2‰ for $\delta^{13}\text{C}_{\text{VPDB}}$. Later dolomite phases (Dol-2 and Dol-3) display $\delta^{18}\text{O}$ values from
455 17.3‰ to 28.6‰ VSMOW and $\delta^{13}\text{C}$ values ranging from -7.8‰ to 2.1‰ VPDB. Based on
456 $\delta^{13}\text{C}$ values, there is a slight distinction between the Dol-2 cement in the host rock (average
457 value: $-0.04 \pm 0.40\text{‰}$ VPDB) and the heavier $\delta^{13}\text{C}$ values of the vein filling Dol-2 (mainly
458 represented by Dol-2b; average value: $1.01 \pm 0.95\text{‰}$ VPDB; Fig. 11). Vein-filling Dol-3 shows
459 the lightest $\delta^{13}\text{C}$ values (Fig. 11). Some values are heavier, but this may likely be due to
460 impurities in Dol-2 during the analysis. For Dol-2 and Dol-3, both $\delta^{13}\text{C}$ and $\delta^{18}\text{O}$ values
461 evolve simultaneously towards lighter isotopic values. Late calcite cements display values
462 ranging from 19.5 to 23.1‰ for $\delta^{18}\text{O}$ and from -8.5 to -6.1‰ for $\delta^{13}\text{C}$ (Fig. 11).

463 5. DISCUSSION

464 5.1. Paragenetic sequence

465 The formation of the Mn(-Fe) ores of Bou Arfa can be summarized in three main
466 stages: (i) Mn-Fe protore, (ii) main Mn-Fe ore and (iii) post ore (Fig. 4). The second stage is
467 economically the most important accounting for most of the extracted Mn ore in the Bou Arfa
468 district, which is mainly expressed by the occurrence of massive pyrolusite. The multistage
469 deposition of Mn-bearing minerals was accompanied by several dolomitization synchronous
470 with the first two stages of Mn deposition (Fig. 4).

471 5.1.1 Mn-Fe protore

472 Manganite and hausmannite (Figs. 6F, 7A, B, C) accompany Dol-2, along with colloform to
473 specular Mn-rich Fe oxyhydroxides (goethite and hematite) and barite (Fig. 4). This early
474 Mn(-Fe) mineralization is mainly observed in the Ain Beida site (Fig. 1B), but the occurrence
475 of hausmannite in the Hamaraouet area also indicates that early stage of mineralization has
476 a larger extension.

477 5.1.2 Main Mn ore

478 Fracture-filling and karst mineralization are later than Dol-2. Pyrolusite is the only Mn oxide
479 (Figs. 3E, 6A, B, F, G and H) and occurs alongside Si-rich goethite, hematite and Mn-
480 dolomite to Ca-rhodochrosite (Fig. 4). The massive pyrolusite shows a wide range of textures
481 from tiny micrometric needles to large prismatic millimetric crystals (Figs. 3E, 6B and F).
482 Variation of pyrolusite bonds in Raman spectra (Fig. 6D) are interpreted as replacement of

483 manganite (Gaudefroy, 1960; Hewett, 1972; Pasero, 2005; Post, 1999; Yoshino et al., 1993,
484 1992). Prismatic pyrolusite is frequently related to manganite replacement (Fleischer et al.,
485 1962). The replacement of Mn²⁺- or Mn³⁺-bearing minerals by pyrolusite enhances the Jahn
486 Teller deformation pattern by including a c-axis elongated Mn³⁺-octahedra in the pyrolusite
487 structure (Julien et al., 2004; Post, 1999; Post et al., 2003; Zwicker et al., 1962). These
488 textures indicate that this mineralization stage impregnates the host rock dolostone and
489 support that pyrolusite partly replaced manganite. Also important is that pyrolusite remains
490 stable and does not accommodate any supplementary cation other than Mn in its structure,
491 unlike manganite, for which substitutions are facilitated by its layer structure (Post, 1999;
492 Post et al., 2003). Conversion from manganite to pyrolusite explains Si, Al and Ca (>2 wt.%)
493 enrichment in pyrolusite (Tables 3 and 5). Mn-Fe oxides precipitated from a similar
494 mineralizing fluid, although Si-rich Fe oxides formed later than pyrolusite (Fig. 7E). This
495 means that this second ore formation stage partly reworks the early mineralization episode.
496 Although, pyrolusite by replacement of manganite is well documented in the Bou Arfa ore,
497 the main ore consists of open-space filling of pyrolusite (Figs. 6A and F). Botryoidal-hematite,
498 proto-hematite and goethite formed later than Dol-2 and destabilized some dolomitic phases
499 (Fig. 4).

500 5.1.3 Late stage supergene enrichment

501 The post-ore supergene stage is poorly expressed in the Bou Arfa ores (Fig. 4). This
502 feature is due to the stability of the main ore-forming minerals under surface or near-surface
503 conditions (Post, 1999), such as pyrolusite and Fe oxides. Some typical supergene minerals
504 have unevenly precipitated as chalcophanite or hollandite-cryptomelane (Figs. 6F, 7A and B)
505 in partial replacement of hausmannite. Chalcophanite is a common weathering product in Mn
506 and Zn deposits (Decrée et al., 2010, 2008; Ostwald, 1992; Post, 1999), and its relation with
507 hausmannite is due to little amounts of Zn (0.3 wt.%; Table 5). Pyrolusite is also partially
508 destabilized and transformed into coronadite group minerals (here hollandite and
509 cryptomelane) as it is often the case in the weathering zone of Mn deposits (Ostwald, 1992;
510 Varentsov, 1996). Late calcite cement (Figs. 3E and F) is also associated with the Mn
511 supergene assemblage and extensively develops in the host rock and mineralization (Fig. 4).
512 The meteoric origin of calcite is supported by partial dedolomitisation (Fig. 3E; Ayora et al.
513 1998; Dewaide et al. 2014) and light isotopic values (Fig. 11).

514 **5.2 Metallogenic model**

515 5.2.1 Metal source(s) in seawater

516 All mineralization, whatever their stage, display similar geochemical patterns (Fig.
517 10B), close to the signal of the host rock dolostone (Figs. 10A and B). It implies that the three
518 ore stages have a similar origin and that the later stages rework an early stock. Chalcophile
519 (As, Zn, Pb, Cu, Ni, Co, V) and some mobile elements (Sr, Ba, Be; Table 3; Figs. 10A and B)
520 are particularly enriched in the orebodies. However, a Principal Component Analysis (PCA)
521 also links As, V, Mo, Co, Ni, Ba, Zn, Sr, Pb, U to the Mn orebodies, unlike immobile and
522 lithophile, which characterize the host Sinemurian dolostone and the Pliensbachian arkoses
523 (Fig. 12A). This indicates that the Mn ore involves external inputs of Mn and associated
524 metals, i.e. from basement rocks. Therefore, it is likely that upward (hot?) mineralizing fluids
525 additionally participated to the ore formation, for example by mixing with shallower
526 oxygenated ground waters, which might explain the karst-like mineralization (Varentsov,
527 1996). This is materialized in Nicholson's diagnostic plots by a clear hydrothermal trend of
528 the Bou Arfa ores (Figs. 12B; Fig. 12C). In addition, this highlights the difference between the
529 Bou Arfa Mn ores from other carbonate-hosted Mn deposits in Morocco (Fig. 12C; Gutzmer
530 et al. 2006; Dekoninck et al. 2016b, a, 2020).

531 5.2.2 Syn-sedimentary and early diagenetic (pre)concentration

532 The occurrence of evaporitic levels, pisoids, oncoids, bird eyes and micro-saccharoidal
533 dolomite (Dol-1; Fig. 3) supports a restricted lagoonal environment, part of the platform
534 interior. This restricted lagoon is protected from open marine environments by an ooid and
535 bioclastic sand shoal, probably forming the platform margin 4-5 km south of the Mn ore
536 deposit of Aïn Beida, in the Jbel Bou Mokhta (Fig. 1B). These restricted lagoonal
537 environments are particularly suitable for early dolomitization (Fig. 4; Land 1985; Jones and
538 Renault 1994; Machel 2004; Arenas-Abad et al. 2010). The oxygen composition of Dol-1 are
539 higher than most common lagoonal dolomite (Blaise et al., 2014; Brigaud et al., 2018;
540 Mauger and Compton, 2011; Ren and Jones, 2017), but they are consistent with shallow
541 depth Mn-rich dolomite (Burns and Baker 1987; Fig. 11). Dolomite (Dol-1) is less abundant in
542 shoal and upper slope facies outside the Bou Arfa (Jbel Bou Mokhta; Figs. 1B, 3G and H).

543 In these shallow marine to lagoonal environments, anoxic to suboxic basins or microbial
544 activity are the most suitable trap for Mn (Folk and Chafetz, 2000; Jones and Renault, 1994;
545 Mandernack et al., 1995b, 1995a; Ostwald, 1990). Microbial activity is usually observed
546 through the coalescence of Mn-Fe-rich pisoid laminae in sedimentary Mn deposits (Groote
547 Eylandt, Chinese, Brazil deposits; Force and Cannon 1988; Frakes and Bolton 1992;
548 Ostwald 1992; Fan and Yang 1999; Fan et al. 1999; Biondi et al. 2020). The absence of Mn-
549 rich or Fe-rich laminae and $\delta^{13}\text{C}$ isotopic values of Dol-1 greater than 0‰ VPDB (Fig. 11) are
550 not consistent with Mn and Fe enrichment by bacteria-mediated organic matter degradation

551 (i.e., black shales; Okita et al. 1988; Polgári et al. 1991, 2012; Fan et al. 1999; Maynard
552 2014; Johnson et al. 2016). Alternatively, the C-O evolutionary trend shown in Figure 11
553 could be interpreted as resulting from fluid mixing between deep upward migrating warm
554 basinal brines and downward infiltration of later cooler meteoric fluid. However, C-rich layers
555 (i.e., coal, lignite) are not present in the sedimentary series. A second dolomitization episode
556 is recorded by Dol-2, although no textural argument clearly establishes if this second event
557 belongs to an early diagenesis or epigenesis (Fig. 5).

558 The high Mn contents of Dol-1 (up to 1.58 ± 0.51 wt.% MnO in Dol-1; Table 4) suggests
559 an early Mn enrichment (Fig. 9C) under suboxic conditions with the absence Fe sulfides or
560 Fe carbonates (Maynard 2014). Without any contribution of organic matter in the Mn fixation,
561 an extremely high alkaline and anoxic to dysoxic environment (0-0.4 Eh) would prevail.
562 Anoxic-suboxic events related to the closure of a narrow and shallow Bou Arfa basin (Piqué
563 et al., 2000; Yelles-Chaouche et al., 2001) may trap the dissolved Mn^{2+} in pore waters. The
564 porosity increased thanks to the early dolomitization and transformation of the earliest
565 carbonates into dolomite. The high Mg:Mn ratio favors precipitation of dolomite with little
566 amounts of Mn, the major part staying in the pore fluid (Table 2). Burial of the Sinemurian
567 sediments would reinforce suboxic conditions that precipitate Mn^{2+} from pore waters into
568 “reduced” Mn oxides (Mn^{2+} and Mn^{3+}), when alkaline conditions are maintained. The high As
569 content in goethite (Table 6) is also consistent with a precipitation under alkaline and suboxic
570 conditions (Campbell and Nordstrom, 2014; Pierce and Moore, 1982). At the same time,
571 dolomitization continued, increasing the porosity of the host rock, and helped to
572 accommodate CO_3^{2-} from pore waters into dolomite phase. The extensive pseudomorphosis
573 between dolomite generations during the ore formation (Figs. 3 and 4) may have limited
574 massive release of CO_3^{2-} in pore waters, and have prevented the formation of Mn-rich
575 carbonates (i.e., Ca-rhodochrosite or kutnohorite; Fig. 4). Only alteration of this primary ore
576 assemblage led to Ca-rhodochrosite (Figs. 4 and 7C; Maynard 2014; Manceau et al. 2014).
577 Consequently, hausmannite and manganite precipitated instead of Mn carbonates. The
578 presence of Mn-rich Fe oxides in the primary stage also indicates a local separation of Fe
579 from Mn at macro/microscopic scale. However, the high Mn content in goethite shows that
580 Fe and Mn probably came with the same mineralizing fluid, but have precipitated separate
581 phases, in different proportions. It likely suggests that the mineralizing fluids carried Mn and
582 Fe with a very low Fe/Mn ratio (Table 6; Fig. 9C).

583 5.2.3 Late diagenetic evolution and hydrothermal circulation during burial

584 The synchronous precipitation of manganite, hausmannite and barite in Mn deposits
585 are commonly attributed to thermal conditions with temperatures much higher (250-350°C)

586 than at the surface (Fan et al., 1999; Gutzmer and Beukes, 1996; Hewett, 1972). Dol-2b and
587 Dol-3 display sub-planar to saddle texture (Figs. 3C and F) due to an increase of
588 temperature (Blaise et al., 2014; Radke and Mathis, 1980; Searl, 1989). Decrease of the
589 $\delta^{18}\text{O}$ values and slight decrease of $\delta^{13}\text{C}$ values from Dol-1 to Dol-2 (Fig. 9) is characteristic of
590 an isotopic re-equilibration triggered by a temperature increase (Brand and Veizer, 1981; Lee
591 and Friedman, 1987; Nader et al., 2007, 2006; Warren, 2000). Moreover, $\delta^{18}\text{O}$ and $\delta^{13}\text{C}$
592 values of the saddle dolomite (Dol-3) are among the lightest (Fig. 9) and support a
593 continuous increase in temperature along the formation of the dolomite generations, and
594 consequently along the formation of the Bou Arfa Mn(-Fe) ores. The saddle dolomite (Dol-3b)
595 originates from a thermal effect instead of oversaturation of Mg (Searl, 1989; Warren, 2000).
596 The temperature allowing non-planar dolomite (Dol-2b) is close to 50°C and a temperature of
597 60°C to 80°C is needed for the saddle dolomite formation (Dol-3b; Radke and Mathis 1980;
598 Machel 2000; Warren 2000). This thermal effect is also shown through the crystallography of
599 Fe oxides (Fig. 8; Table 9). In experiments, the formation of proto-hematite occurs beyond
600 ~140°C (Wolska and Schwertmann, 1989) and the short a axis of the goethite cell at Bou
601 Arfa (Table 9) testifies to the higher formation temperatures (>50°C; Schwertmann et al.
602 1985). This interpretation is further supported by the evolutionary trend shown by the
603 distribution of C and O isotopic data (Fig. 11) and an important change in $\delta^{13}\text{C}$ from the
604 classical burial diagenesis in Dol 3. This involves warm basinal brines and their subsequent
605 mixing with downward percolating cooler meteoric fluids. The E-W-trending Aïn Beida fault
606 zone would have enhanced the widespread infiltration of meteoric fluids. These observations
607 indicate that burial and additional hot fluids are the driver for late dolomitization (Dol-2 and
608 Dol-3) and Fe oxide stages (Fig. 5). It is materialized by karst and vein mineralization (Fig.
609 6A, F, 6A, B and C) and by mineralogical transformations of the primary ore (Fig. 5). The
610 successive dolomite generations are similar to the burial model of Cu-Co deposits described
611 in the Central Africa Copper Belt (Dewaele et al., 2006; El Desouky et al., 2009; Hoy and
612 Ohmoto, 1989). The formation of Mn-rich dolomite and Ca-rhodochrosite are also indicators
613 of burial diagenesis in the Bou Arfa deposit (Fig. 4). Actually, the reductive conditions related
614 to burial and the loss of oxygen renewal is suitable for the partial manganite degradation into
615 Ca-rhodochrosite (Fig. 7C; Roy 2006; Johnson et al. 2016).

616 Consequently, the genesis of the remobilized ore (Fig. 5) might be due to (i)
617 remobilization of the primary ore and (ii) migration of Mn by diagenetically-driven
618 hydrothermal fluids. The Aïn Beida fault (Fig. 1B) played an important role by facilitating
619 fracturation of the host rock and enhancing Mn-bearing fluid circulation. It is not excluded that
620 hausmannite and manganite resulted from the transformation of former Mn oxides. Such
621 mineral evolution is common in hypogene and metamorphic Mn deposits (Hewett 1972;

622 Nicholson 1992; Gutzmer et al. 1995; Post 1999). There are few petrographical arguments
623 pleading for the presence of an early Mn carbonate precursor as formerly presented by Pouit
624 and Jouravsky (1965).

625 5.2.4. The Cenozoic Atlas exhumation: supergene enrichment

626 Hollandite, cryptomelane and chalcophanite (Figs. 6F and G) were accompanied by
627 dedolomitisation (Fig. 4E). These late meteoric fluids have not substantially enriched the Bou
628 Arfa ore, except maybe for Zn that was concentrated in chalcophanite, and Sr in hollandite-
629 cryptomelane (Table 3). The supergene origin of the Fe oxides is unlikely with their
630 crystallographic features (Fig. 8; Table 9) and explains why these minerals have precipitated
631 later than manganite, hausmannite and pyrolusite. This relatively poor weathering is quite
632 contrasting with the numerous Cu-Zn-Pb-V hypogene deposits of the eastern High Atlas and
633 Anti-Atlas, where an oxidation zone systematically occurs (Bouabdellah et al., 2012; Choulet
634 et al., 2014; Poot et al., 2020; Rddad and Bouhleb, 2016; Verhaert et al., 2018, 2017). The
635 weathering phase recorded in the Bou Arfa ores is probably connected to the repeated
636 exhumation of the Atlas since late Cretaceous times (Dekoninck et al., 2020; Frizon de
637 Lamotte et al., 2000; Froitzheim, 1984; Leprêtre et al., 2018, 2015).

638 **5.3 Place of the Mn Bou Arfa deposit in the Mesozoic evolution of the Atlas**

639 Without geochronological constraints, the absolute timing of the Bou Arfa Mn(-Fe)
640 mineralization is difficult to establish, but has seemingly occurred after the deposition of the
641 Sinemurian carbonates. Sinemurian dolostones were deposited in the context of rifting and
642 deepening of several sedimentary basins along the Atlas belt (Frizon de Lamotte et al., 2009;
643 Nottvedt et al., 1995; Teixell et al., 2009; White and McKenzie, 1988). This setting would
644 explain the position of the Bou Arfa Mn deposit, as the basin could act as a threshold, given
645 its location above a paleohigh. The strong variation in the thickness of the sedimentary series
646 in the Bou Arfa basin indicates an important variation of the geometry and/or significant
647 lateral variation of the sedimentary facies that would have delimited the extension of the Mn
648 mineralization (Torres-Ruiz, 1983). This sharp transition of sedimentary facies is well
649 demonstrated in the Jbel Bou Moktha (Fig. 1B), where the Sinemurian carbonate facies
650 evolves from a lagoonal (dolomitic-peloidal facies) to an offshore environment
651 (marls/limestones alternations). Transgression events during the Sinemurian interval
652 repeatedly supplied dissolved Mn^{2+} , and when the Bou Arfa area was isolated from seawater
653 influxes, was trapped in pore waters. The situation of the Bou Arfa deposit in a narrow basin
654 pinched to the north by the Tendirara rift shoulder and to the south by a narrow ditch (Tamlet
655 plain; Piqué et al. 2000; Yelles-Chaouche et al. 2001) was an efficient trap for dolomitization
656 and Mn pre-concentration. The position of the deposit above paleohigh basement rocks and

657 close to a major tectonic thrust (Fig. 1B) have provided suitable conditions for brecciation
658 and fracturing enhancing diagenetically-driven hydrothermal circulation in porous Sinemurian
659 dolostones.

660 The metallogenesis of the Bou Arfa ores is different from the high-grade Imini-Tasdremt Mn
661 deposits (Figs. 12B and C). Accordingly, the Imini-Tasdremt Mn ores postdate the latest
662 meteoric dolomite generation and do not show any Mn precursor (Dekoninck et al., 2016a)
663 nor saddle dolomite (Force et al., 1986). Moreover, the host dolostone is intensely karstified
664 with dissolution and collapse breccia filled by sands (Gutzmer et al., 2006) and the age of the
665 Mn ore span over a period of ~25 Ma during the late Cretaceous (Dekoninck et al., 2020).
666 The accepted formation model of the Imini-Tasdremt ores involves mixing of O₂-rich meteoric
667 waters and acidic O₂-free ground waters (Gutzmer et al., 2006). For these reasons, the
668 comparison between these two carbonate-hosted Mn deposits is unfaithful although the
669 dolomitic trap has some similarities, i.e. the isotopic composition (Fig. 11) and Fe:Mn ratios
670 (Fig. 9C) of the host dolostones.

671 **5.4. Relation of the Bou Arfa Mn(-Fe) ores with Mississippi Valley Type deposits in** 672 **North Africa**

673 Mississippi Valley Type (MVT) deposits are widespread along Meso-Cenozoic shallow-water
674 carbonate platforms forming the Atlas system (Bouabdellah and Sangster, 2016; Decrée et
675 al., 2016). The occurrence of numerous Pb-Zn MVT and Cu mineralization in Jurassic series
676 of the Bou Arfa region (Fig. 1; e.g., Chefchaouni et al. 1963; Verhaert et al. 2017, 2018) also
677 supports the predominant role of dolostone in trapping various metals. The Bou Arfa deposit
678 is comparable with major Zn-Pb MVT deposits of Morocco (Bouabdellah et al., 2015, 2012;
679 Bouabdellah and Sangster, 2016; Jébrak et al., 1998; Rddad, 2021; Rddad et al., 2018;
680 Rddad and Bouhleb, 2016) at several levels: (1) they are hosted in Lower to Middle Jurassic
681 unmetamorphosed platform carbonate rocks; (2) the mineralization fills open spaces (veins,
682 interconnected cavities, solution-collapse breccias) and replaces carbonate; (3) the
683 mineralization is accompanied by different generations of saddle dolomite or calcite; (4) the
684 deposits are located above basement paleohighs where Triassic to Jurassic rocks are
685 pinched out; and (5) the ENE-WSW and E-W faults have facilitated fluid circulation in
686 permeable rocks hosting the ore. The genesis of Pb-Zn MVT mineralization in Morocco is
687 explained by ascending diagenetically-derived hydrothermal solutions due to compaction
688 and/or gravity-driven systems mixing with surficial cooler fluids. The mineralizing fluids were
689 forced to spread laterally along the porous Lower and Middle Jurassic aquifer due to Upper
690 Jurassic cap rock (Bouabdellah and Sangster, 2016). MVT deposits are likely formed before
691 the onset of the non-sulphide supergene ores supposed at ~20 Ma (Choulet et al., 2014;

692 Verhaert et al., 2017). The heat source for MVT deposits in the Atlas range may derived from
693 the Alpine orogenesis itself that caused large-scale fluid circulation of deep-seated fluids
694 rather than direct volcanic activities (Rddad, 2021). The High Atlas has indeed a thin
695 lithosphere supported by a thermal anomaly since the Miocene (Leprêtre et al., 2018 and
696 reference therein), which has provided proper thermal conditions for various mineralization
697 types in the High Atlas. Such interpretation can be applied to the Bou Arfa Mn(-Fe) deposit.

698 **6. CONCLUSIONS**

699 This study emphasizes the role of dolomitization in the formation of the Bou Arfa Mn(-
700 Fe) deposit. The accumulation of the Bou Arfa Mn ores follows a multistage genesis in close
701 association with three dolomite events. Early diagenesis (Dol-1 and Dol-2) and epigenesis
702 (Dol-3) are associated with the mineralization process by providing suitable conditions for Mn
703 oxides precipitation instead of Mn carbonates. The porosity, depletion in dissolved carbonate
704 species in pore waters and suboxic conditions are responsible for the primary hausmannite,
705 manganite, barite and (Mn-)goethite assemblage. The subsequent burial of the host
706 Sinemurian dolostone is clearly observed through (i) a textural evolution from non-planar
707 (Dol-2b) to saddle dolomite (Dol-3), (ii) a decrease in the $\delta^{13}\text{C}$ and $\delta^{18}\text{O}$ isotopic values and
708 (iii) crystallographic changes of the Fe oxides. This increase in temperature and pressure
709 triggered mineralogical transformations of the primary manganite into massive pyrolusite with
710 (Si-)goethite, hematite and (Mn-)dolomite to Ca-rhodochrosite, whereas hausmannite
711 remained stable. Diagenetically-driven hydrothermal circulation, enhanced by the vicinity of
712 the Aïn Beida fault, is responsible for the formation of deep karst and vein-type Mn and then
713 Fe ores. A mixing fluid model is also suitable for the late evolution of the Mn mineralization. It
714 emphasizes that goethite and some of the Mn oxides, commonly attributed to strictly
715 supergene conditions, were formed under higher temperatures ($>50^\circ\text{C}$). The supergene
716 contribution is very low given the stability of the ore-forming minerals under supergene
717 conditions. Weathering only proceeded through partial replacement of hausmannite (and
718 rarely pyrolusite) into chalcophanite and coronadite group minerals.

719 The Bou Arfa deposit can be considered as a diagenetic deposit showing similarities
720 with MVT deposits of North Africa, where a predominant role is played by dolomitization. In
721 the context of global extension (opening of Tethys) forming several Jurassic basins along the
722 High Atlas, the Bou Arfa area played differently due to local settings. This narrow basin lying
723 above a paleohigh basement in a heavily faulted zone probably facilitated circulation of
724 diagenetic fluids and strictly delimited the geometry of the Mn ores. Transgression-regression
725 intervals determined the input of dissolved Mn into the basin.

726 **Acknowledgement**

727 We warmly thank the Caïdat of Bou Arfa and the ONHYM for giving access to outcrops and
 728 samples. We are grateful to Michel Dubois, head manager of the CGCE laboratory of the
 729 University of Lille 1 (France) for helping us in the acquisition of Raman spectra. We greatly
 730 appreciated the help of Gaëtan Rochez for taking field pictures and collecting samples. This
 731 research did not receive any specific grant from funding agencies in the public, commercial,
 732 or not-for-profit sectors. Michèle Verhaert thanks the Belgian Fund for Scientific Research
 733 (FNRS) for providing a FRIA PhD grant.

734 References

- 735 Arenas-Abad, C., Vázquez-Urbez, M., Pardo-Tirapu, G., Sancho-Marcén, C., 2010. Chapter
 736 3 Fluvial and Associated Carbonate Deposits, in: *Developments in Sedimentology*.
 737 Elsevier, pp. 133–175. [https://doi.org/10.1016/S0070-4571\(09\)06103-2](https://doi.org/10.1016/S0070-4571(09)06103-2)
- 738 Ayora, C., Taberner, C., Saaltink, M.W., Carrera, J., 1998. The genesis of dedolomites: a
 739 discussion based on reactive transport modeling. *Journal of Hydrology* 209, 346–365.
 740 [https://doi.org/10.1016/S0022-1694\(98\)00095-X](https://doi.org/10.1016/S0022-1694(98)00095-X)
- 741 Biondi, J.C., Polgári, M., Gyollai, I., Fintor, K., Kovács, I., Fekete, J., Mojzsis, S.J., 2020.
 742 Biogenesis of the Neoproterozoic kremydilite manganese ores from Urucum (Brazil) –
 743 A new manganese ore type. *Precambrian Research* 340, 105624.
 744 <https://doi.org/10.1016/j.precamres.2020.105624>
- 745 Blaise, T., Barbarand, J., Kars, M., Ploquin, F., Aubourg, C., Brigaud, B., Cathelineau, M., El
 746 Albani, A., Gautheron, C., Izart, A., Janots, D., Michels, R., Pagel, M., Pozzi, J.-P.,
 747 Boiron, M.-C., Landrein, P., 2014. Reconstruction of low temperature (<100 °C) burial
 748 in sedimentary basins: A comparison of geothermometer in the intracontinental Paris
 749 Basin. *Marine and Petroleum Geology* 53, 71–87.
 750 <https://doi.org/10.1016/j.marpetgeo.2013.08.019>
- 751 Bouabdellah, M., Niedermann, S., Velasco, F., 2015. The Touissit-Bou Beker Mississippi
 752 Valley-Type District of Northeastern Morocco: Relationships to the Messinian Salinity
 753 Crisis, Late Neogene-Quaternary Alkaline Magmatism, and Buoyancy-Driven Fluid
 754 Convection. *Economic Geology* 110, 1455–1484.
 755 <https://doi.org/10.2113/econgeo.110.6.1455>
- 756 Bouabdellah, M., Sangster, D.F., 2016. Geology, Geochemistry, and Current Genetic Models
 757 for Major Mississippi Valley-Type Pb–Zn Deposits of Morocco, in: Bouabdellah, M.,
 758 Slack, J.F. (Eds.), *Mineral Deposits of North Africa*, Mineral Resource Reviews.
 759 Springer International Publishing, Cham, pp. 463–495. https://doi.org/10.1007/978-3-319-31733-5_19
- 761 Bouabdellah, M., Sangster, D.F., Leach, D.L., Brown, A.C., Johnson, C.A., Emsbo, P., 2012.
 762 Genesis of the Touissit-Bou Beker Mississippi Valley-Type District (Morocco-Algeria)
 763 and Its Relationship to the Africa-Europe Collision. *Economic Geology* 107, 117–146.
 764 <https://doi.org/10.2113/econgeo.107.1.117>
- 765 Brand, J., Veizer, J., 1980. Chemical diagenesis of a multicomponent carbonate system:
 766 trace elements. *SEPM Journal of Sedimentary Research* Vol. 50.
 767 <https://doi.org/10.1306/212F7BB7-2B24-11D7-8648000102C1865D>
- 768 Brand, U., Veizer, J., 1981. Chemical diagenesis of a multicomponent carbonate system; 2,
 769 Stable isotopes. *Journal of Sedimentary Research* 51, 987–997.
 770 <https://doi.org/10.1306/212F7DF6-2B24-11D7-8648000102C1865D>
- 771 Brigaud, B., Vincent, B., Pagel, M., Gras, A., Noret, A., Landrein, P., Huret, E., 2018.
 772 Sedimentary architecture, depositional facies and diagenetic response to intracratonic
 773 deformation and climate change inferred from outcrops for a pivotal period
 774 (Jurassic/Cretaceous boundary, Paris Basin, France). *Sedimentary Geology* 373, 48–
 775 76. <https://doi.org/10.1016/j.sedgeo.2018.04.011>

- 776 Burns, S.J., Baker, P.A., 1987. A geochemical study of dolomite in the Monterey Formation,
777 California. *Journal of Sedimentary Research* 57, 128–139.
778 <https://doi.org/10.1306/212F8AC6-2B24-11D7-8648000102C1865D>
- 779 Calvert, S.E., Pedersen, T.F., 1996. Sedimentary geochemistry of manganese; implications
780 for the environment of formation of manganese-rich black shales. *Economic Geology*
781 91, 36–47. <https://doi.org/10.2113/gsecongeo.91.1.36>
- 782 Campbell, K.M., Nordstrom, D.K., 2014. Arsenic Speciation and Sorption in Natural
783 Environments. *Reviews in Mineralogy and Geochemistry* 79, 185–216.
784 <https://doi.org/10.2138/rmg.2014.79.3>
- 785 Cannon, W.F., Force, E.R., 1983. Potential for high-grade shallow-marine manganese
786 deposits in North America, in: *Cameron Volume on Unconventional Mineral Deposits*.
787 American Institute of Mining, Metallurgical and Petroleum Engineers, New York, NY,
788 pp. 175–189.
- 789 Chefchaoui, Y.C., Diouri, M., Choubert, G., 1963. Carte géologique de la France à 1/50
790 000, 341, Gérardmer. *Notes et mémoires du Service géologique du Maroc*.
- 791 Choubert, G., Faure-Muret, A., 1973. The Precambrian iron and manganese deposits of the
792 Anti-Atlas, in: *Genesis of Precambrian Iron and Manganese Deposits*. Presented at
793 the Unesco Earth Sciences Symposium, Kiev, pp. 115–124.
- 794 Choubert, G., Faure-Muret, A., 1962. Evolution du domaine atlasique marocain depuis les
795 temps paléozoïques, in: *Livre à La Mémoire Du Professeur Paul Fallot, Mémoire Hors*
796 *Série*. Société Géologique de France, Paris, pp. 447–527.
- 797 Choulet, F., Charles, N., Barbanson, L., Branquet, Y., Sizaret, S., Ennaciri, A., Badra, L.,
798 Chen, Y., 2014. Non-sulfide zinc deposits of the Moroccan High Atlas: Multi-scale
799 characterization and origin. *Ore Geology Reviews* 56, 115–140.
800 <https://doi.org/10.1016/j.oregeorev.2013.08.015>
- 801 Cornell, R.M., Schwertmann, U., 2003. *The Iron Oxides: Structure, Properties, Reactions,*
802 *Occurrences and Uses*, 1st ed. Wiley. <https://doi.org/10.1002/3527602097>
- 803 de Wolff, P.M.D., 1959. Interpretation of some γ -MnO₂ diffraction patterns. *Acta*
804 *Crystallographica* 12, 341–345. <https://doi.org/10.1107/S0365110X59001001>
- 805 Decrée, S., De Putter, T., Yans, J., Moussi, B., Recourt, P., Jamoussi, F., Bruyère, D.,
806 Dupuis, C., 2008. Iron mineralisation in Mio-Pliocene sediments of the Tamra iron
807 mine (Nefza mining district, Tunisia): Mixed influence of pedogenesis and
808 hydrothermal alteration. *Ore Geology Reviews* 33, 397–410.
809 <https://doi.org/10.1016/j.oregeorev.2007.02.001>
- 810 Decrée, S., Marignac, C., Abidi, R., Jemmali, N., Deloule, E., Souissi, F., 2016.
811 Tectonomagmatic Context of Sedex Pb–Zn and Polymetallic Ore Deposits of the
812 Nappe Zone Northern Tunisia, and Comparisons with MVT Deposits in the Region, in:
813 Bouabdellah, M., Slack, J.F. (Eds.), *Mineral Deposits of North Africa*. Springer
814 International Publishing, Cham, pp. 497–525. https://doi.org/10.1007/978-3-319-31733-5_20
- 815
816 Decrée, S., Ruffet, G., Putter, T.D., Baele, J.-M., Recourt, P., Jamoussi, F., Yans, J., 2010.
817 Mn oxides as efficient traps for metal pollutants in a polyphase low-temperature
818 Pliocene environment: A case study in the Tamra iron mine, Nefza mining district,
819 Tunisia. *Journal of African Earth Sciences* 57, 249–261.
820 <https://doi.org/10.1016/j.jafrearsci.2009.08.005>
- 821 Dekoninck, A., Bernard, A., Barbarand, J., Saint-Bezar, B., Missenard, Y., Lepretre, R.,
822 Saddiqi, O., Yans, J., 2016a. Detailed mineralogy and petrology of manganese
823 oxyhydroxide deposits of the Imini district (Morocco). *Mineralium Deposita* 51, 13–23.
824 <https://doi.org/10.1007/s00126-015-0590-3>
- 825 Dekoninck, A., Lepretre, R., Saddiqi, O., Barbarand, J., Yans, J., 2016b. The high-grade
826 Imini manganese district—karst-hosted deposits of Mn oxides and oxyhydroxides, in:
827 Bouabdellah, M., Slack, J.F. (Eds.), *Mineral Deposits of North Africa*. Springer
828 International Publishing, Cham, pp. 575–594.
- 829 Dekoninck, A., Ruffet, G., Missenard, Y., Parizot, O., Magoua, M., Mouttaqi, A., Rochez,
830 Gaëtan, Yans, J., 2020. Multistage genesis of the late Cretaceous manganese karst-

- 831 hosted Tasdremt deposit (High Atlas, Morocco). *Mineralium Deposita*.
 832 <https://doi.org/10.1007/s00126-020-01017-0>
- 833 Dewaele, S., Muchez, Ph., Vets, J., Fernandez-Alonzo, M., Tack, L., 2006. Multiphase origin
 834 of the Cu–Co ore deposits in the western part of the Lufilian fold-and-thrust belt,
 835 Katanga (Democratic Republic of Congo). *Journal of African Earth Sciences* 46, 455–
 836 469. <https://doi.org/10.1016/j.jafrearsci.2006.08.002>
- 837 Dewaide, L., Baele, J.-M., Collon-Drouaillet, P., Quinif, Y., Rochez, G., Vandycke, S., Hallet,
 838 V., 2014. Karstification in dolomitized Waulsortian mudmounds (Belgium). *Geologica*
 839 *Belgica* 17, 43–51.
- 840 du Dresnay, R., 1965. Notice géologique sur la région de Bou-Arfa – Colloque sur les gîtes
 841 stratiformes de plomb, zinc et manganèse du Maroc (2 mai - 14 mai 1962). *Notes et*
 842 *Mémoires du Service Géologique du Maroc* 181, 107–112.
- 843 El Desouky, H.A., Muchez, P., Cailteux, J., 2009. Two Cu–Co sulfide phases and contrasting
 844 fluid systems in the Katanga Copperbelt, Democratic Republic of Congo. *Ore*
 845 *Geology Reviews* 36, 315–332. <https://doi.org/10.1016/j.oregeorev.2009.07.003>
- 846 Fan, D., Yang, P., 1999. Introduction to and classification of manganese deposits of China.
 847 *Ore Geology Reviews* 15, 1–13. [https://doi.org/10.1016/S0169-1368\(99\)00011-6](https://doi.org/10.1016/S0169-1368(99)00011-6)
- 848 Fan, D., Ye, J., Li, J., 1999. Geology, mineralogy, and geochemistry of the Middle
 849 Proterozoic Wafangzi ferromanganese deposit, Liaoning Province, China. *Ore*
 850 *Geology Reviews* 15, 31–53. [https://doi.org/10.1016/S0169-1368\(99\)00013-X](https://doi.org/10.1016/S0169-1368(99)00013-X)
- 851 Fleet, A.J., 1983. Hydrothermal and Hydrogenous Ferro-Manganese Deposits: Do They form
 852 a Continuum? The Rare Earth Element Evidence, in: Rona, P.A., Boström, K.,
 853 Laubier, L., Smith, K.L. (Eds.), *Hydrothermal Processes at Seafloor Spreading*
 854 *Centers*. Springer US, Boston, MA, pp. 535–555. https://doi.org/10.1007/978-1-4899-0402-7_23
- 856 Fleischer, M., Richmond, W.E., Evans, H.T., 1962. Studies of manganese oxides. 5.
 857 Ramsdellite MnO₂, an orthorhombic dimorph of pyrolusite. *American Mineralogist* 47,
 858 47–58.
- 859 Folk, R.L., Chafetz, H.S., 2000. Bacterially Induced Microscale and Nanoscale Carbonate
 860 Precipitates, in: Riding, R.E., Awramik, S.M. (Eds.), *Microbial Sediments*. Springer,
 861 Berlin, Heidelberg, pp. 40–49. https://doi.org/10.1007/978-3-662-04036-2_6
- 862 Force, E.R., Back, W., Spiker, E.C., Knauth, L.P., 1986. A ground-water mixing model for the
 863 origin of the Imini manganese deposit (Cretaceous) of Morocco. *Economic Geology*
 864 81, 65–79. <https://doi.org/10.2113/gsecongeo.81.1.65>
- 865 Force, E.R., Cannon, W.F., 1988. Depositional model for shallow-marine manganese
 866 deposits around black shale basins. *Economic Geology* 83, 93–117.
 867 <https://doi.org/10.2113/gsecongeo.83.1.93>
- 868 Force, E.R., Maynard, J.B., 1991. Manganese: Syngenetic deposits on the margins of anoxic
 869 basins, in: *Sedimentary and Diagenetic Mineral Deposits: A Basin Analysis Approach*
 870 *to Exploration*. Society of Economic Geologists, Littleton, Colorado, pp. 147–159.
- 871 Frakes, L., Bolton, B.R., 1992. Effects of ocean chemistry, sea level, and climate on the
 872 formation of primary sedimentary manganese ore deposits. *Economic Geology* 87,
 873 1207–1217. <https://doi.org/10.2113/gsecongeo.87.5.1207>
- 874 Frizon de Lamotte, D., Leturmy, P., Missenard, Y., Khomsi, S., Ruiz, G., Saddiqi, O.,
 875 Guillocheau, F., Michard, A., 2009. Mesozoic and Cenozoic vertical movements in the
 876 Atlas system (Algeria, Morocco, Tunisia): An overview. *Tectonophysics* 475, 9–28.
 877 <https://doi.org/10.1016/j.tecto.2008.10.024>
- 878 Frizon de Lamotte, D., Saint Bezar, B., Bracène, R., Mercier, E., 2000. The two main steps of
 879 the Atlas building and geodynamics of the western Mediterranean. *Tectonics* 19,
 880 740–761. <https://doi.org/10.1029/2000TC900003>
- 881 Froitzheim, N., 1984. Late Cretaceous vertical tectonics in the High Atlas SW of
 882 Marrakech/Morocco - Reconstruction of tectonic movements in an early stage of the
 883 High Atlas orogenesis. *Neu Jb Paläont Mh* 463–471.
- 884 Fu, Q., Qing, H., Bergman, K.M., 2006. Early dolomitization and recrystallization of carbonate
 885 in an evaporite basin: the Middle Devonian Ratner laminite in southern

- 886 Saskatchewan, Canada. *Journal of the Geological Society* 163, 937–948.
887 <https://doi.org/10.1144/0016-76492005-088>
- 888 Gao, T., Fjellvåg, H., Norby, P., 2009. A comparison study on Raman scattering properties of
889 α - and β -MnO₂. *Analytica Chimica Acta* 648, 235–239.
890 <https://doi.org/10.1016/j.aca.2009.06.059>
- 891 Gasparrinia, M., Bakker, R.J., Bechstdt, Th., Boni, M., 2003. Hot dolomites in a Variscan
892 foreland belt: hydrothermal flow in the Cantabrian Zone (NW Spain). *Journal of*
893 *Geochemical Exploration, Proceedings of Geofluids IV* 78–79, 501–507.
894 [https://doi.org/10.1016/S0375-6742\(03\)00115-8](https://doi.org/10.1016/S0375-6742(03)00115-8)
- 895 Gaudefroy, G., 1960. Caractères distinctifs de la pyrolusite - ex manganite (application au
896 minerai de l'Imini). *Notes du Service Géologique Marocain* 19, 77–86.
- 897 Glasby, G.P., 2006. Manganese: Predominant Role of Nodules and Crusts, in: Schulz, H.D.,
898 Zabel, M. (Eds.), *Marine Geochemistry*. Springer-Verlag, Berlin/Heidelberg, pp. 371–
899 427. https://doi.org/10.1007/3-540-32144-6_11
- 900 Gouiza, M., Charton, R., Bertotti, G., Andriessen, P., Storms, J.E.A., 2017. Post-Variscan
901 evolution of the Anti-Atlas belt of Morocco constrained from low-temperature
902 geochronology. *International Journal of Earth Sciences* 106, 593–616.
903 <https://doi.org/10.1007/s00531-016-1325-0>
- 904 Gualtieri, A.F., Venturelli, P., 1999. In situ study of the goethite-hematite phase
905 transformation by real time synchrotron powder diffraction. *American Mineralogist* 84,
906 895–904. <https://doi.org/10.2138/am-1999-5-624>
- 907 Gutzmer, J., Beukes, N.J., 1996. Mineral paragenesis of the Kalahari manganese field,
908 South Africa. *Ore Geology Reviews* 11, 405–428. [https://doi.org/10.1016/S0169-1368\(96\)00011-X](https://doi.org/10.1016/S0169-1368(96)00011-X)
- 910 Gutzmer, J., Beukes, N.J., Kleyenstuber, A.S.E., Burger, A.M., 1995. Magnetic hausmannite
911 from hydrothermally altered manganese ore in the Palaeoproterozoic Kalahari
912 manganese deposit, Transvaal Supergroup, South Africa. *Mineralogical Magazine* 59,
913 703–716. <https://doi.org/10.1180/minmag.1995.059.397.12>
- 914 Gutzmer, J., Beukes, N.J., Rhalimi, M., Mukhopadhyay, J., 2006. Cretaceous karstic cave-fill
915 manganese-lead-barium deposits of Imini, Morocco. *Economic Geology* 101, 385–
916 405. <https://doi.org/10.2113/gsecongeo.101.2.385>
- 917 Hewett, D.F., 1972. Manganite, hausmannite, braunite: features, modes of origin. *Economic*
918 *Geology* 67, 83–102. <https://doi.org/10.2113/gsecongeo.67.1.83>
- 919 Hoy, L.D., Ohmoto, H., 1989. Constraints for the genesis of redbed associated stratiform Cu
920 deposits from sulphur and carbon mass balance relations, in: Boyle, R.W., Brown,
921 A.C., Jefferson, C.W., Jowett, E.C., Kirkham, R.V. (Eds.), *Sediment-Hosted Stratiform*
922 *Copper Deposits*. St. John's, pp. 135–149.
- 923 Jébrak, M., Marcoux, É., Nasloubi, M., Zaharaoui, M., 1998. From sandstone- to carbonate-
924 hosted stratabound deposits: an isotope study of galena in the Upper-Moulouya
925 District (Morocco). *Mineral. Deposita* 33, 406–415.
926 <https://doi.org/10.1007/s001260050158>
- 927 Johnson, J.E., Webb, S.M., Ma, C., Fischer, W.W., 2016. Manganese mineralogy and
928 diagenesis in the sedimentary rock record. *Geochimica et Cosmochimica Acta* 173,
929 210–231. <https://doi.org/10.1016/j.gca.2015.10.027>
- 930 Jones, B., Renaut, R.W., 1994. Crystal fabrics and microbiota in large pisoliths from Laguna
931 Pastos Grandes, Bolivia. *Sedimentology* 41, 1171–1202.
932 <https://doi.org/10.1111/j.1365-3091.1994.tb01448.x>
- 933 Julien, C., Massot, M., Rangan, S., Lemal, M., Guyomard, D., 2002. Study of structural
934 defects in γ -MnO₂ by Raman spectroscopy. *Journal of Raman Spectroscopy* 33,
935 223–228. <https://doi.org/10.1002/jrs.838>
- 936 Julien, C.M., Massot, M., Poinsignon, C., 2004. Lattice vibrations of manganese oxides: Part
937 I. Periodic structures. *Spectrochimica Acta Part A: Molecular and Biomolecular*
938 *Spectroscopy* 60, 689–700. [https://doi.org/10.1016/S1386-1425\(03\)00279-8](https://doi.org/10.1016/S1386-1425(03)00279-8)

- 939 Kuleshov, V., 2016. Isotope geochemistry: the origin and formation of manganese rocks and
940 ores. Elsevier, Amsterdam Boston Heidelberg London New York Oxford Paris San
941 Diego San Francisco Singapore Sydney Tokyo.
- 942 Kuleshov, V.N., 2011. Manganese deposits: Communication 1. Genetic models of
943 manganese ore formation. *Lithology and Mineral Resources* 46, 473–493.
944 <https://doi.org/10.1134/S0024490211050038>
- 945 Lafforgue, L., 2016. Place de la minéralisation de manganèse de Bouarfa dans l'évolution
946 méso-cénozoïque de l'oriental marocain (PhD). Université Paris Sud, Paris.
- 947 Land, L.S., 1985. The Origin of Massive Dolomite. *Journal of Geological Education* 33, 112–
948 125. <https://doi.org/10.5408/0022-1368-33.2.112>
- 949 Langford, J.I., Wilson, A.J.C., 1978. Scherrer after sixty years: A survey and some new
950 results in the determination of crystallite size. *J Appl Cryst* 11, 102–113.
951 <https://doi.org/10.1107/S0021889878012844>
- 952 Laznicka, P., 1992. Manganese deposits in the global lithogenetic system: Quantitative
953 approach. *Ore Geology Reviews* 7, 279–356. [https://doi.org/10.1016/0169-
954 1368\(92\)90013-B](https://doi.org/10.1016/0169-1368(92)90013-B)
- 955 Lee, Y.I., Friedman, G.M., 1987. Deep-burial dolomitization in the Ordovician Ellenburger
956 Group carbonates, West Texas and southeastern New Mexico. *Journal of
957 Sedimentary Research* 57, 544–557. [https://doi.org/10.1306/212F8B8E-2B24-11D7-
958 8648000102C1865D](https://doi.org/10.1306/212F8B8E-2B24-11D7-8648000102C1865D)
- 959 Leprêtre, R., Missenard, Y., Barbarand, J., Gautheron, C., Jouvie, I., Saddiqi, O., 2018.
960 Polyphased inversions of an intracontinental rift: case study of the Marrakech High
961 Atlas, Morocco. *Tectonics* 37, 818–841. <https://doi.org/10.1002/2017TC004693>
- 962 Leprêtre, R., Missenard, Y., Saint-Bezar, B., Barbarand, J., Delpech, G., Yans, J.,
963 Dekoninck, A., Saddiqi, O., 2015. The three main steps of the Marrakech High Atlas
964 building in Morocco: Structural evidences from the southern foreland, Imini area.
965 *Journal of African Earth Sciences* 109, 177–194.
966 <https://doi.org/10.1016/j.jafrearsci.2015.05.013>
- 967 Lima-de-Faria, J., 1963. Dehydration of goethite and diaspore. *Zeitschrift für Kristallographie
968 - Crystalline Materials* 119, 176–203. <https://doi.org/10.1524/zkri.1963.119.3-4.176>
- 969 Machel, H.G., 2004. Concepts and models of dolomitization: a critical reappraisal. *Geological
970 Society, London, Special Publications* 235, 7–63.
971 <https://doi.org/10.1144/GSL.SP.2004.235.01.02>
- 972 Machel, H.G., 2000. Application of Cathodoluminescence to Carbonate Diagenesis, in:
973 Pagel, M., Barbin, V., Blanc, P., Ohnenstetter, D. (Eds.), *Cathodoluminescence in
974 Geosciences*. Springer Berlin Heidelberg, Berlin, Heidelberg, pp. 271–301.
975 https://doi.org/10.1007/978-3-662-04086-7_11
- 976 Manceau, A., Lanson, M., Takahashi, Y., 2014. Mineralogy and crystal chemistry of Mn, Fe,
977 Co, Ni, and Cu in a deep-sea Pacific polymetallic nodule. *American Mineralogist* 99,
978 2068–2083. <https://doi.org/10.2138/am-2014-4742>
- 979 Mandernack, K.W., Fogel, M.L., Tebo, B.M., Usui, A., 1995a. Oxygen isotope analyses of
980 chemically and microbially produced manganese oxides and manganates.
981 *Geochimica et Cosmochimica Acta* 59, 4409–4425. [https://doi.org/10.1016/0016-
982 7037\(95\)00299-F](https://doi.org/10.1016/0016-7037(95)00299-F)
- 983 Mandernack, K.W., Post, J., Tebo, B.M., 1995b. Manganese mineral formation by bacterial
984 spores of the marine *Bacillus*, strain SG-1: Evidence for the direct oxidation of Mn(II)
985 to Mn(IV). *Geochimica et Cosmochimica Acta* 59, 4393–4408.
986 [https://doi.org/10.1016/0016-7037\(95\)00298-E](https://doi.org/10.1016/0016-7037(95)00298-E)
- 987 Mattauer, M., Tapponnier, P., Proust, F., 1977. Sur les mecanismes de formation des
988 chaines intracontinentales; l'exemple des chaines atlasiques du Maroc. *Bulletin de la
989 Société Géologique de France* S7-XIX, 521–526.
990 <https://doi.org/10.2113/gssgfbull.S7-XIX.3.521>
- 991 Mauger, C.L., Compton, J.S., 2011. Formation of modern dolomite in hypersaline pans of the
992 Western Cape, South Africa. *Sedimentology* 58, 1678–1692.
993 <https://doi.org/10.1111/j.1365-3091.2011.01229.x>

- 994 Maynard, J.B., 2014. Manganiferous sediments, rocks, and ores, in: *Treatise on*
995 *Geochemistry*. Elsevier, pp. 327–349.
- 996 Maynard, J.B., 2010. The chemistry of manganese ores through time: a signal of increasing
997 diversity of earth-surface environments. *Economic Geology* 105, 535–552.
998 <https://doi.org/10.2113/gsecongeo.105.3.535>
- 999 Meister, P., Reyes, C., 2019. The Carbon-Isotope Record of the Sub-Seafloor Biosphere.
1000 *Geosciences* 9, 507. <https://doi.org/10.3390/geosciences9120507>
- 1001 Michard, A., Raddi, Y., 2011. Le manganèse de Bou-Arfa (Haut Atlas oriental), in: Mouttaqi,
1002 A., Rjimati, E.C., Maacha, L., Michard, André, Soulaïmani, A., Ibouh, H. (Eds.), *Les*
1003 *Principales Mines Du Maroc, Notes et Mémoires Du Service Géologique. Notes et*
1004 *mémoires du service géologique*, Rabat, pp. 305–308.
- 1005 Missenard, Y., Saddiqi, O., Barbarand, J., Leturmy, P., Ruiz, G., El Haimer, F.-Z., Frizon de
1006 Lamotte, D., 2008. Cenozoic denudation in the Marrakech High Atlas, Morocco:
1007 insight from apatite fission-track thermochronology. *Terra Nova* 20, 221–228.
1008 <https://doi.org/10.1111/j.1365-3121.2008.00810.x>
- 1009 Missenard, Y., Zeyen, H., Frizon de Lamotte, D., Leturmy, P., Petit, C., Sébrier, M., Saddiqi,
1010 O., 2006. Crustal versus asthenospheric origin of relief of the Atlas Mountains of
1011 Morocco. *Journal of Geophysical Research: Solid Earth* 111, n/a-n/a.
1012 <https://doi.org/10.1029/2005JB003708>
- 1013 Montanez, I.P., Read, J.F., 1992. Fluid-rock interaction history during stabilization of early
1014 dolomites, upper Knox Group (Lower Ordovician), U.S. Appalachians. *Journal of*
1015 *Sedimentary Research* 62, 753–778. [https://doi.org/10.1306/D42679D3-2B26-11D7-](https://doi.org/10.1306/D42679D3-2B26-11D7-8648000102C1865D)
1016 [8648000102C1865D](https://doi.org/10.1306/D42679D3-2B26-11D7-8648000102C1865D)
- 1017 Mouttaqi, A., Rjimati, E.C., Maacha, L., Michard, A., Soulaïmani, A., Ibouh, H., 2011. *Les*
1018 *principales mines du Maroc, Editions du Service Géologique du Maroc. ed, New*
1019 *geological and mining guidebooks of Morocco. Ministère de l'Energie, des Mines, de*
1020 *l'Eau et de l'Environnement*, Rabat.
- 1021 Nader, F.H., Swennen, R., Ellam, R.M., 2006. Petrographic and geochemical study of
1022 Jurassic dolostones from Lebanon: Evidence for superimposed diagenetic events.
1023 *Journal of Geochemical Exploration, GEOFLUIDS V: 5th International Conference on*
1024 *Fluid Evolution, Migration and Interaction in Sedimentary Basins and Orogenic Belts*
1025 89, 288–292. <https://doi.org/10.1016/j.gexplo.2005.11.003>
- 1026 Nader, F.H., Swennen, R., Ellam, R.M., Immenhauser, A., 2007. Field geometry, petrography
1027 and geochemistry of a dolomitization front (Late Jurassic, central Lebanon).
1028 *Sedimentology* 54, 1093–1120. <https://doi.org/10.1111/j.1365-3091.2007.00874.x>
- 1029 Nicholson, K., 1992. Contrasting mineralogical-geochemical signatures of manganese
1030 oxides; guides to metallogenesis. *Economic Geology* 87, 1253–1264.
1031 <https://doi.org/10.2113/gsecongeo.87.5.1253>
- 1032 Nottvedt, A., Gabrielsen, R.H., Steel, R.J., 1995. Tectonostratigraphy and sedimentary
1033 architecture of rift basins, with reference to the northern North Sea. *Marine and*
1034 *Petroleum Geology, Integrated Basin Studies* 12, 881–901.
1035 [https://doi.org/10.1016/0264-8172\(95\)98853-W](https://doi.org/10.1016/0264-8172(95)98853-W)
- 1036 Okita, P.M., Maynard, J.B., Spiker, E.C., Force, E.R., 1988. Isotopic evidence for organic
1037 matter oxidation by manganese reduction in the formation of stratiform manganese
1038 carbonate ore. *Geochimica et Cosmochimica Acta* 52, 2679–2685.
1039 [https://doi.org/10.1016/0016-7037\(88\)90036-1](https://doi.org/10.1016/0016-7037(88)90036-1)
- 1040 Ostwald, J., 1992. Genesis and paragenesis of the tetravalent manganese oxides of the
1041 Australian continent. *Economic Geology* 87, 1237–1252.
1042 <https://doi.org/10.2113/gsecongeo.87.5.1237>
- 1043 Ostwald, J., 1990. The biogeochemical origin of the Groote Eylandt manganese oxide
1044 pisoliths and ooliths, northern Australia. *Ore Geology Reviews, Palynology of ore*
1045 *deposits* 5, 469–490. [https://doi.org/10.1016/0169-1368\(90\)90048-R](https://doi.org/10.1016/0169-1368(90)90048-R)
- 1046 Pasero, M., 2005. A Short Outline of the Tunnel Oxides. *Reviews in Mineralogy and*
1047 *Geochemistry* 57, 291–305. <https://doi.org/10.2138/rmg.2005.57.9>

- 1048 Pierce, M.L., Moore, C.B., 1982. Adsorption of arsenite and arsenate on amorphous iron
1049 hydroxide. *Water Research* 16, 1247–1253. [https://doi.org/10.1016/0043-](https://doi.org/10.1016/0043-1354(82)90143-9)
1050 [1354\(82\)90143-9](https://doi.org/10.1016/0043-1354(82)90143-9)
- 1051 Piqué, A., Charroud, M., Laville, E., Ait Brahim, L., Amrhar, M., 2000. The Tethys southern
1052 margin in Morocco; Mesozoic and Cenozoic evolution of the Atlas domain, in:
1053 Crasquin-Soleau, S., Barrier, E. (Eds.), *New Data on Peri-Tethyan Sedimentary*
1054 *Basins*. Publications scientifiques du Muséum, Paris, pp. 93–106.
- 1055 Polgári, M., Hein, J.R., Vigh, T., Szabó-Drubina, M., Fórizs, I., Bíró, L., Müller, A., Tóth, A.L.,
1056 2012. Microbial processes and the origin of the Úrkút manganese deposit, Hungary.
1057 *Ore Geology Reviews* 47, 87–109. <https://doi.org/10.1016/j.oregeorev.2011.10.001>
- 1058 Polgári, M., Okita, P.M., Hein, J.R., 1991. Stable Isotope evidence for the origin of the Urkut
1059 Manganese ore deposit, Hungary. *SEPM Journal of Sedimentary Research* 61.
1060 <https://doi.org/10.1306/D426771C-2B26-11D7-8648000102C1865D>
- 1061 Pomiès, M.P., Morin, G., Vignaud, C., 1998. XRD study of the goethite-hematite
1062 transformation: Application to the identification of heated prehistoric pigments.
1063 *European Journal of Solid State and Inorganic Chemistry* 35, 9–25.
1064 [https://doi.org/10.1016/S0992-4361\(98\)80011-8](https://doi.org/10.1016/S0992-4361(98)80011-8)
- 1065 Poot, J., Verhaert, M., Dekoninck, A., Oummouch, A., El Basbas, A., Maacha, L., Yans, J.,
1066 2020. Characterization of Weathering Processes of the Giant Copper Deposit of
1067 Tizert (Igherm Inlier, Anti-Atlas, Morocco). *Minerals* 10, 620.
1068 <https://doi.org/10.3390/min10070620>
- 1069 Post, J.E., 1999. Manganese oxide minerals: crystal structures and economic and
1070 environmental significance. *Proceedings of the National Academy of Sciences* 96,
1071 3447–3454. <https://doi.org/10.1073/pnas.96.7.3447>
- 1072 Post, J.E., Heaney, P.J., Hanson, J., 2003. Synchrotron X-ray diffraction study of the
1073 structure and dehydration behavior of todorokite. *American Mineralogist* 88, 142–150.
1074 <https://doi.org/10.2138/am-2003-0117>
- 1075 Pouit, G., 1980. Manganèse. *Notes et Mémoires du Service Géologique du Maroc*, Rabat 13,
1076 61–67.
- 1077 Pouit, G., 1964. Les gîtes de manganèse marocains encaissés dans les Formations
1078 carbonatées : éléments pour une synthèse. *Chronique des Mines et de la Recherche*
1079 *Minière* 371–380.
- 1080 Pouit, G., Jouravsky, G., 1965. Les minéralisations manganésifères de la région de Bou-Arfa
1081 - Colloque sur les gites stratiformes de plomb, zinc, et manganèse du Maroc. *Notes*
1082 *et Mémoires du Service Géologique du Maroc* 181, 113–131.
- 1083 Radke, B.M., Mathis, R.L., 1980. On the formation and occurrence of saddle dolomite.
1084 *Journal of Sedimentary Research* 50, 1149–1168. [https://doi.org/10.1306/212F7B9E-](https://doi.org/10.1306/212F7B9E-2B24-11D7-8648000102C1865D)
1085 [2B24-11D7-8648000102C1865D](https://doi.org/10.1306/212F7B9E-2B24-11D7-8648000102C1865D)
- 1086 Rddad, L., 2021. The genesis of the Jurassic-hosted Mississippi Valley-type Pb-Zn ore
1087 deposit, Tigrinine-Taabast district (Central High Atlas, Morocco): Insights from fluid
1088 inclusion and C-O-S-Pb isotope studies. *Journal of African Earth Sciences* 174,
1089 104071. <https://doi.org/10.1016/j.jafrearsci.2020.104071>
- 1090 Rddad, L., Bouhlef, S., 2016. The Bou Dahar Jurassic carbonate-hosted Pb–Zn–Ba deposits
1091 (Oriental High Atlas, Morocco): Fluid-inclusion and C–O–S–Pb isotope studies. *Ore*
1092 *Geology Reviews* 72, 1072–1087. <https://doi.org/10.1016/j.oregeorev.2015.08.011>
- 1093 Rddad, L., Mouguina, E.M., Muchez, P., Darling, R.S., 2018. The genesis of the Ali Ou
1094 Daoud Jurassic carbonate Zn-Pb Mississippi Valley-type deposit, Moroccan central
1095 High Atlas: Constraints from bulk stable C-O-S, in situ radiogenic Pb isotopes, and
1096 fluid inclusion studies. *Ore Geology Reviews* 99, 365–379.
1097 <https://doi.org/10.1016/j.oregeorev.2018.06.020>
- 1098 Ren, M., Jones, B., 2017. Spatial variations in the stoichiometry and geochemistry of
1099 Miocene dolomite from Grand Cayman: Implications for the origin of island dolostone.
1100 *Sedimentary Geology* 348, 69–93. <https://doi.org/10.1016/j.sedgeo.2016.12.001>

- 1101 Rendon, J.L., Cornejo, J., de Arambarri, P., 1983. Grinding-induced effects on goethite (α -
 1102 FeOOH). *Journal of Colloid and Interface Science* 94, 546–551.
 1103 [https://doi.org/10.1016/0021-9797\(83\)90294-1](https://doi.org/10.1016/0021-9797(83)90294-1)
- 1104 Roy, S., 2006. Sedimentary manganese metallogenesis in response to the evolution of the
 1105 Earth system. *Earth-Science Reviews* 77, 273–305.
 1106 <https://doi.org/10.1016/j.earscirev.2006.03.004>
- 1107 Salahane, A., 1978. Etude géologique et métallogénique du gisement cuprifère du Jbel Klakh
 1108 Haut Atlas oriental (Maroc): Contribution à la métallogénie paléokarstique. *Notes et*
 1109 *Mémoires du Service Géologique du Maroc* 40, 147–237.
- 1110 Scherrer, P., 1918. Estimation of the size and internal structure of colloidal particles by
 1111 means of röntgen. *Nachrichten von der Gesellschaft der Wissenschaften zu Göttingen*
 1112 *Mathematisch-Physikalische Klasse*, 2, 96–100.
- 1113 Schwertmann, U., Cambier, P., Murad, E., 1985. Properties of Goethites of Varying
 1114 Crystallinity. *Clays Clay Miner.* 33, 369–378.
 1115 <https://doi.org/10.1346/CCMN.1985.0330501>
- 1116 Searl, A., 1989. Saddle dolomite: a new view of its nature and origin. *Mineralogical Magazine*
 1117 53, 547–555. <https://doi.org/10.1180/minmag.1989.053.373.05>
- 1118 Searl, A., Fallick, A.E., 1990. Dinantian dolomites from East Fife: hydrothermal overprinting
 1119 of early mixing-zone stable isotopic and Fe/Mn compositions. *Journal of the*
 1120 *Geological Society* 147, 623–638. <https://doi.org/10.1144/gsjgs.147.4.0623>
- 1121 Seber, D., Barazangi, M., Tadili, B.A., Ramdani, M., Ibenbrahim, A., Ben Sari, D., 1996.
 1122 Three-dimensional upper mantle structure beneath the intraplate Atlas and interplate
 1123 Rif mountains of Morocco. *Journal of Geophysical Research: Solid Earth* 101, 3125–
 1124 3138. <https://doi.org/10.1029/95JB03112>
- 1125 Teixell, A., Bertotti, G., de Lamotte, D.F., Charroud, M., 2009. The geology of vertical
 1126 movements of the lithosphere: An overview. *Tectonophysics* 475, 1–8.
 1127 <https://doi.org/10.1016/j.tecto.2009.08.018>
- 1128 Torres-Ruiz, J., 1983. Genesis and evolution of the Marquesado and adjacent iron ore
 1129 deposits, Granada, Spain. *Economic Geology* 78, 1657–1673.
 1130 <https://doi.org/10.2113/gsecongeo.78.8.1657>
- 1131 Varentsov, I.M., 1996. Manganese ores of supergene zone: Geochemistry of formation, *Solid*
 1132 *Earth Sciences Library*. Springer Netherlands, Dordrecht.
- 1133 Verhaert, M., Bernard, A., Dekoninck, A., Lafforgue, L., Saddiqi, O., Yans, J., 2017.
 1134 Mineralogical and geochemical characterization of supergene Cu–Pb–Zn–V ores in
 1135 the Oriental High Atlas, Morocco. *Mineralium Deposita*.
 1136 <https://doi.org/10.1007/s00126-017-0753-5>
- 1137 Verhaert, M., Bernard, A., Saddiqi, O., Dekoninck, A., Essalhi, M., Yans, J., 2018. Mineralogy
 1138 and Genesis of the Polymetallic and Polyphased Low Grade Fe-Mn-Cu Ore of Jbel
 1139 Rhals Deposit (Eastern High Atlas, Morocco). *Minerals* 8, 39.
 1140 <https://doi.org/10.3390/min8020039>
- 1141 Walter, D., Buxbaum, G., Laqua, W., 2001. The Mechanism of the Thermal Transformation
 1142 From Goethite to Hematite. *Journal of Thermal Analysis and Calorimetry* 63, 733–
 1143 748. <https://doi.org/10.1023/A:1010187921227>
- 1144 Wang, X., Müller, W.E.G., 2009. Marine biominerals: perspectives and challenges for
 1145 polymetallic nodules and crusts. *Trends in Biotechnology* 27, 375–383.
 1146 <https://doi.org/10.1016/j.tibtech.2009.03.004>
- 1147 Warren, J., 2000. Dolomite: occurrence, evolution and economically important associations.
 1148 *Earth-Science Reviews* 52, 1–81. [https://doi.org/10.1016/S0012-8252\(00\)00022-2](https://doi.org/10.1016/S0012-8252(00)00022-2)
- 1149 White, N., McKenzie, D., 1988. Formation of the steer's head geometry of sedimentary
 1150 basins by differential stretching of the crust and mantle. *Geology* 16, 250–253.
 1151 [https://doi.org/10.1130/0091-7613\(1988\)016<0250:FOTSSH>2.3.CO;2](https://doi.org/10.1130/0091-7613(1988)016<0250:FOTSSH>2.3.CO;2)
- 1152 Wolska, E., Schwertmann, U., 1989. Nonstoichiometric structures during dehydroxylation of
 1153 goethite. *Zeitschrift für Kristallographie - Crystalline Materials* 189, 223–237.
 1154 <https://doi.org/10.1524/zkri.1989.189.3-4.223>

- 1155 Wolska, E., Szajda, W., 1988. The effect of cationic and anionic substitution on the α -(Al,
1156 Fe) $_2$ O $_3$ lattice parameters. *Solid State Ionics* 28–30, 1320–1323.
1157 [https://doi.org/10.1016/0167-2738\(88\)90379-7](https://doi.org/10.1016/0167-2738(88)90379-7)
- 1158 Yelles-Chaouche, A.K., Ait Ouali, R., Bracene, R., Derder, M.E.M., Djellit, H., 2001.
1159 Chronologie de l'ouverture du bassin des Ksour (Atlas Saharien, Algerie) au debut du
1160 Mesozoique. *Bulletin de la Société Géologique de France* 172, 285–293.
1161 <https://doi.org/10.2113/172.3.285>
- 1162 Yoshino, T., Miura, H., Hariya, Y., 1993. Crystal structure of orthorhombic pyrolusite from
1163 Imini mine, in: Ishihara, S., Urabe, T., Ohmoto, H. (Eds.), *Mineral Resources*
1164 *Symposia*. Society of Resource Geologists of Japan, Tokyo, pp. 62–65.
- 1165 Yoshino, T., Miura, H., Hariya, Y., 1992. Crystal structure of orthorhombic pyrolusite, in:
1166 *Abstract Book*. Presented at the International Geological Congress, Kyoto, p. 216.
- 1167 Zenger, D.H., Dunham, J.B., Ethington, R.L. (Eds.), 1980. *Concepts and Models of*
1168 *Dolomitization*. SEPM (Society for Sedimentary Geology).
1169 <https://doi.org/10.2110/pec.80.28>
- 1170 Zwicker, W.K., Groeneveld-Meijer, W.O.J., Jaffe, H.W., 1962. Nsutite - a widespread
1171 manganese oxide mineral. *American Mineralogist* 47, 618–623.
1172

1173 Figures

1174 **Fig. 1 (color).** **A.** Simplified structural map of Morocco showing the location of Mn
1175 mineralization. MA= Middle Atlas, EHA=Eastern High Atlas, HA= High Atlas, WHA=Western
1176 High Atlas, SAF=South Atlas Front, NAF=North Atlas Front. **B.** Local geological map of the
1177 Bou Arfa cliff and the Mn mineralization (modified after Pouit and Jouravsky 1965). H1-
1178 4=Hamaraouet, HB=Hamarouet and Aïn Beida, 63= Gallery 63.

1179 **Fig. 2 (black and white).** Stratigraphic column of the Tamlet area (left) and in the
1180 Hamaraouet sector (right).

1181 **Fig. 3 (color).** Petrographic views of carbonate generations in the host rock. **A.** CL view of a
1182 sandstone level at the base of the UCU cemented by Dol-1a (sample J2-2). **B.** Oolith
1183 replaced by Dol-1a and cemented by Dol-1b under CL at the bottom of the UCU. **C.**
1184 Successive generations of dolomite crystals filling fractures and void in H2 (sample H2 – Dol
1185 – Min). **D.** Bird eyes facies in the UCU dolostone at Hamaraouet (H1) crisscrossed by
1186 several calcite veins. **E.** Dedolomitization of Dol-2A in the Mn ore at Hamaraouet (H3) with
1187 pyrolusite crystals. **F.** Late calcite filling void at Hamaraouet (sample H2-Br-Dol). **G.** Early
1188 dolomite generation with ferrous (Cal-1a) and non-ferrous (Cal-1b) calcites in the UCU of the
1189 Jbel Bou Moktha under PPL prepared with a mix of alizarine-red and K-ferricyanide. **H.** Late
1190 calcite generations in the UCU of Jbel Bou Moktha under CL. Dol=dolomite, Py=pyrolusite,
1191 Ca=calcite.

1192 **Fig. 4 (color).** Tentative paragenetic sequence of the Bou Arfa deposit. Schematic
1193 petrographic reconstruction of dolomite generations is given for cement and veins (see Table
1194 6 for key features of dolomite generations).

1195 **Fig. 5 (color).** Field observations of the Mn and Fe ores. See location on Fig. 1B. **A.**
 1196 Galleries in the Hamaraouet area (H1) in the Upper “Chocolate” Unit. **B.** View of the Aïn
 1197 Beida mining site and the Bou Arfa cliff. **C.** Stratabound orebody in gallery 63. **D.** Stockwork
 1198 in the host UCU dolostone between Aïn Beida and Hamaraouet (HB). **E.** Mn and Fe oxides in
 1199 the Hamaraouet area (H1). **F.** Massive goethite vein in the Hamaraouet area (H3). **G.** Fe
 1200 oxide vein crossing the stratabound Mn ore in gallery 63. **H.** Stockwork of pyrolusite in the
 1201 UCU in Hamaraouet (H3).

1202 **Fig. 6 (color).** Petrographic views of main mineralization types. **A.** Cluster mineralization
 1203 showing pyrolusite veins crossing early dolomite generation (Dol-1 and 2) filled by calcite
 1204 under SEM-BSE view at Hamaraouet. **B.** Disseminated bipyramidal pyrolusite growing onto
 1205 altered Dol-2B and cemented by coarse Dol-3B under SEM-BSE view at H2 (sample H2-Dol-
 1206 Min). **C.** Cluster mineralization showing needles and fusiform pyrolusite in gallery 63 under
 1207 NAPL. **D.** Raman spectra for pyrolusite in gallery 63 (63-01_3D1, 63-01_2D1) and between
 1208 Hamaraouet and Aïn Beida (HA; HAB_1D1). **E.** Pyrolusite growing onto early botryoidal
 1209 goethite generation in gallery 63 under NAPL. **F.** Pyrolusite and cryptomelane crossing
 1210 hausmannite crystals and Dol-3 under SEM-BSE view at Hamaraouet (H1-Min2).
 1211 Hausmannite is partly weathered into chalcophanite. Note that pyrolusite, in turn, seems to
 1212 partly weathers into cryptomelane. **G.** Late botryoidal goethite brecciated by Dol-3A
 1213 generation under SEM-BSE view at Hamaraouet. Note that late goethite grows onto the
 1214 pyrolusite-calcite matrix. **H.** SEM-BSE view of hausmannite filled by Dol-3b and pyrolusite.
 1215 Hollandite partly replaces pyrolusite. Dol=dolomite, Cal=calcite, Py=pyrolusite,
 1216 Cph=chalcophanite, Hs=hausmannite, Cry=cryptomelane, Gth=goethite, Hol=hollandite.

1217 **Fig. 7 (color).** Petrographic views of main mineralization types. **A.** Mixing of different Mn
 1218 oxides (hausmannite, pyrolusite, cryptomelane, chalcophanite) within the host dolostone in
 1219 Hamaraouet (H1) under PPL. **B.** Zoom of Fig. 6A under SEM-BSE showing hausmannite
 1220 replaced by chalcophanite and cryptomelane. Pyrolusite occurs between hausmannite
 1221 crystals. Note that Dol-3 is broken by cryptomelane. **C.** SEM-BSE view showing phase
 1222 relation between hausmannite and manganite crossed by Mn carbonate (Ca-rhodochrosite)
 1223 at Aïn Beida (AB). **D.** SEM-BSE view of crest-like barite associated with manganite and late
 1224 Mn carbonate at Aïn Beida (AB). **E.** Massive late goethite generation growing onto
 1225 hummocky pyrolusite in Hamaraouet (H4). Dol=dolomite, Cal=calcite, Py=pyrolusite,
 1226 Cph=chalcophanite, Hs=hausmannite, Cry=cryptomelane, Gth=goethite, Mnt=manganite,
 1227 Ba=barite, Rh=rhodochrosite.

1228 **Fig. 8 (black and white).** Average integral crystallites of goethite (A) and hematite (B)
 1229 samples.

1230 **Fig. 9 (color).** Geochemistry of dolomite generations (Table 4). **A.** Composition of cement
 1231 dolomite in the host rock. **B.** Composition of vein-filling dolomite. **C.** Distribution of MnO and
 1232 FeO of dolomite in various geological settings. The Bou Arfa dolomite generations display an
 1233 individual trend toward low FeO/MnO ratio.

1234 **Fig. 10 (color).** Trace element pattern of whole rock analyses in the Mn (A) and Fe (B) ores
 1235 (Tables 2 and 3).

1236 **Fig. 11 (color).** Stable isotope (Table 7) plot to show the trend of progressive dolomitization
 1237 in the Bou Arfa Mn deposit. Data from MVT deposits (Bouabdellah et al., 2012; Rddad, 2021;
 1238 Rddad et al., 2018; Rddad and Bouhlel, 2016), Mn Imini deposit (Force et al., 1986) and
 1239 shallow Mn-rich dolomite (Burns and Baker, 1987) are included.

1240 **Fig. 12 (black and white).** **A.** PCA statistical distribution of chemical elements in the Bou
 1241 Arfa deposit. **B-C.** Discrimination plot (Nicholson, 1992) between hydrothermal, supergene
 1242 and dubhite Mn accumulation.

1243 TABLES

1244 **Table 1.** Description and location (Fig. 1B) of the studied samples. The mineralogy is
 1245 referred as Qz=quartz, Fds=feldspars, Zr=zircon, Ap=apatite, Musc=muscovite,
 1246 Dol=dolomite, Bt=biotite, Fe-Ti Ox.= Fe-Ti oxides, Py=pyrolusite, Hs=hausmannite, Fe-ox=
 1247 Fe oxyhydroxides, Cph=chalcophanite, Cpm=cryptomelane, Cal=calcite, Hem=hematite,
 1248 Goe=goethite, Hol=hollandite, Ba=barite. The main minerals are in bolt. WRA is the whole
 1249 rock analysis.

1250 **Table 2.** Whole rock geochemistry (major and trace elements) of the host and basement
 1251 rocks given in wt.% (major oxides and LOI) and ppm (traces). <D.L. is under detection limit.
 1252 LOI is the lost on ignition.

1253 **Table 3.** Whole rock geochemistry (major and trace elements) of the Mn and Fe ores rocks
 1254 given in wt.% (major oxides and LOI) and ppm (traces). <D.L. is under detection limit. LOI is
 1255 the lost on ignition.

1256 **Table 4.** EPMA analyses of different carbonate phases. The average values are given with
 1257 their minimum (min) and maximum (max) values. The number of analyses is mentioned (=n).
 1258 Standard deviation is also indicated for each batch and for the instrument (σ). D.L. is the
 1259 detection limit. Standard list can be found in the data repository.

1260 **Table 5.** EPMA analyses of Mn oxides: hausmannite and pyrolusite in Hamaraouet, and
 1261 supergene cryptomelane, hollandite and chalcophanite. The number of analyses is

1262 mentioned (=n). The average values are given. Standard deviation is also indicated for each
1263 batch and for the instrument (σ). D.L. is the detection limit. Standard list can be found in the
1264 data repository. Standard list can be found in the data repository.

1265 **Table 6.** EPMA analyses of different Fe oxides. The number of analyses is mentioned (=n).
1266 The average values are given. Standard deviation is also indicated for each batch and for the
1267 instrument (σ). D.L. is the detection limit. Standard list can be found in the data repository.

1268 **Table 7.** $\delta^{13}\text{C}$ and $\delta^{18}\text{O}$ compositions of dolomite in the Bou Arfa deposit. See Fig. 1B for the
1269 location of the studied samples.

1270 **Table 8.** Key identification criteria of the dolomite generations under cathodoluminescence
1271 (CL) and light microscopy (LM).

1272 **Table 9.** Cell dimensions of four goethite in Hamaraouet (Fig. 2) following the three main cell
1273 orthorhombic axis. The error is calculated according to the deviation of the experimental
1274 peak from the standard value.

1276 **Supplementary data repository**1277 **DR1.** Analytical conditions standards of the EPMA CAMECA SX-five analyses.1278 **DR2.** Peak features in the XRD patterns of botryoidal hematite (H3_Hem) and across the
1279 massive goethite vein (H3_Gth6-9).

1280 Highlights

- 1281 • The Bou Arfa Mn(-Fe) mineralization (High Atlas, Morocco) is formed by post-
1282 sedimentary processes
- 1283 • Dolomitization is considered as the main driver for Mn and Fe concentration
- 1284 • The stability of the Mn(-Fe)-bearing minerals disabled strong post-ore weathering
- 1285 • The proposed metallogenic model is similar to the genesis of Atlasic MVT deposits

1286